Diagnosis of Broken Bar Fault in Three-Phase Induction Motors Using Fibre Bragg Grating Strain Sensors Assisted by an Algorithm

Rafael Mancuso Paraiso Cavalcanti - 54163

Dissertation presented to the School of Technology and Management of Bragança to obtain the Master's Degree in Industrial Engineering. Work developed during the double degree exchange program between the Polytechnic Institute of Bragança (IPB) and the Federal Technological University of Paraná (UTFPR).

Work oriented by:

Prof. André C. Mendes, D.Sc.

Prof. Kleiton Moraes, D.Sc.

Bragança

September 2023

Diagnosis of Broken Bar Fault in Three-Phase Induction Motors Using Fibre Bragg Grating Strain Sensors Assisted by an Algorithm

Rafael Mancuso Paraiso Cavalcanti - 54163

Dissertation presented to the School of Technology and Management of Bragança to obtain the Master's Degree in Industrial Engineering. Work developed during the double degree exchange program between the Polytechnic Institute of Bragança (IPB) and the Federal Technological University of Paraná (UTFPR).

Work oriented by:

Prof. André C. Mendes, D.Sc.

Prof. Kleiton Moraes, D.Sc.

Bragança

September 2023

Dedication

I dedicate this work to all the people who have been part of my life in some way, especially my close friends and my family.

Acknowledgement

I would like to express my gratitude to everyone who has contributed in any way, both academically and personally, to help me achieve this goal.

I extend a special thank you to Prof. André Mendes and Prof. Kleiton Moraes de Sousa for always being available to assist me with any challenges I faced.

I am thankful to UTFPR and IPB, as well as all the professors who were part of my academic journey during my time at these institutions, for the support they provided me. I would like to specifically mention the Electrical Engineering Department.

To my childhood friends in Frederico Westphalen and the surrounding region, Marcos, Bruno, Ithalo, Daniel, Vínicius, Lucas, and Patrick, who have been my companions since adolescence and have always supported me.

To my friends at UTFPR, who have been by my side throughout my undergraduate studies, studying together during late nights and early mornings, especially the class of 2017/10.

To my friends and companions Cezar, Thales, Jean, Nathan, Renan, and Merce.

To the friends, I made in Bragança, who accompanied me throughout my experience at IPB and in Europe. A special thank you to 3D: Alan, Pedro, Eduardo, and Matheus, and to everyone in the village.

To my family, my father Marcelo, my mother Malva, my sister Clara, and my stepfather Carlos. I would like to mention my mother, who has always supported me and been there for me. She did everything within her reach, and even the impossible, to allow me to pursue a master's degree abroad and complete my undergraduate studies.

Abstract

In this study, we developed an algorithm for identifying failures caused by broken bars in the rotors of three-phase induction motors through the analysis of their dynamic deformation using fibre optic Bragg gratings (FBGs) as sensing elements. The analysis of dynamic deformation enables the detection and diagnosis of various mechanical faults, such as misalignment, imbalance, bearing failures, and mechanical looseness. Furthermore, it allows for the identification of electrical faults, such as fractures or cracks in the rotor rings or bars.

To measure the dynamic deformation, we employed FBG-based sensors known for their key features, including high multiplexing capability, electromagnetic radiation immunity, and long-distance operation. Experimental tests were conducted on a small-scale induction motor (3 HP) to validate the method and explore its applicability to medium and large-scale machines. The motor was powered by two different supply sources: the utility power grid and a controled power sources, under load conditions of 75% and 100% of the rated load.

During the tests, we used a rotor without any bar defects and subsequently a rotor with a broken bar. The presence of a broken bar was successfully identified under both load conditions and across all two power supply sources. The fault caused by the broken bar in the rotor was detected in two frequency regions obtained from the three sets of experiments. The first region was centred around the mechanical rotational frequency of the rotor, while the second region was approximately twice the electrical frequency of the power supply.

The system demonstrated high sensitivity with a good signal-to-noise ratio and showcased advantages over conventional methods and sensors commonly used for identifying broken bar faults in induction motors.

Keywords: Dynamic strain. Induction motor. Rotor broken bar fault. Fiber Bragg gratings. Algorithm.

Resumo

Neste estudo, desenvolvemos um algoritmo para identificar falhas em barras quebradas no rotor de motores de indução trifásicos por meio da análise da deformação dinâmica do estator usando grades de Bragg em fibras ópticas (FBGs) com assitência de um algoritmo. Essa análise possibilita a detecção e o diagnóstico de várias falhas mecânicas, como desalinhamento, desbalanceamento e folga mecânica. Além disso, permite a identificação de falhas elétricas, como fraturas ou rachaduras nos anéis ou barras do rotor.

Para medir a deformação dinâmica, empregamos sensores baseados em FBG conhecidos por suas principais características, incluindo alta capacidade de multiplexação, imunidade à radiação eletromagnética e operação a longa distância. Testes experimentais foram conduzidos em um motor de indução em pequena escala (3 HP) para validar o método e explorar sua aplicabilidade em máquinas de médio e grande porte. O motor foi alimentado por duas fontes de alimentação diferentes: a rede elétrica de utilidade pública e por uma fonte controlada, sob condições de carga de 75% e 100% da carga nominal.

Durante os testes, utilizamos um rotor sem defeitos no rotor e, posteriormente, um rotor com uma barra quebrada. A presença da barra quebrada foi identificada com sucesso em ambas as condições de carga e em todas as duas fontes de alimentação. A barra quebrada no rotor foi detectada em duas regiões de frequência obtidas a partir dos três conjuntos de experimentos. A primeira região estava centrada em torno da frequência rotacional mecânica do rotor, enquanto a segunda região era aproximadamente o dobro da frequência elétrica da fonte de alimentação.

O sistema demonstrou alta sensibilidade com uma boa relação sinal-ruído e apresentou vantagens sobre os métodos convencionais e sensores comumente usados para identificar

falhas em barras quebradas em motores de indução.

Palavras Chave: Deformação dinâmica. Motor de indução. Falha na barra do rotor. Grades de Bragg em fibras ópticas. Algoritmo.

Contents

List of Tables

List of Figures

Acronyms

FBG Fiber Bragg Grating.

FFT Fast Fourier Transform.

HBM Hottinger Baldwin Messtechnik.

IAS Instantaneous Angular Speed.

IPB Polytechnic Institute of Bragança.

MCSA Motor Current Signature Analysis.

PSD Power Spectral Density.

RMS Root mean square.

TIM Three-phase Induction Motor.

UTFPR Federal Technological University of Paraná.

WDM Wavelength Division Multiplexing.

Chapter 1

Introduction

Three-phase induction motors (TIMs) are essential for industrial processes as they convert electrical energy into mechanical energy. They are valued for their simplicity, robustness, versatility, low maintenance requirements, and cost-effectiveness [1]–[3]. Rotating electrical machines consume approximately 50% of the world's electricity, they have become the primary choice in various industries due to advancements in power electronics and digital control, enabling variable-speed operation. Induction motors find extensive use in critical applications such as transportation, healthcare, military operations, telecommunications, aerospace, and nuclear power plants [4].

Despite their reliability, induction motors can experience occasional failures due to factors such as component lifespan, deterioration, contamination, manufacturing defects, or operational damage [5]–[7]. Unexpected motor failures result in maintenance costs, equipment replacement, downtime, and significant losses for industries. In critical sectors like transportation and healthcare, motor failures can even endanger lives. This highlights the necessity for precise fault detection systems [8].

Reliable diagnostic methods for TIM faults rely on understanding their normal electrical, mechanical, and magnetic behaviour. Faults in TIMs can cause changes in magnetic flux behaviour, leading to alterations in stator current, vibration, temperature, noise, and other parameters. The objective is to identify correlations between specific fault types and the resulting disturbances in one or more of these parameters [5], [8].

1.1 Motivation

Failure analysis in electric machines reveals that a significant portion of faults can be attributed to different components. Bearing failures account for approximately 40% to 50% of the total, stator faults range from 30% to 40% and fractures or cracks in the rotor's short-circuit rings or bars contribute to 5% to 10% of failures [5]. The improvement in stator winding design and regular maintenance of bearings have effectively reduced the occurrence of stator and bearing failures. However, this has shifted the focus to rotor failures, which have become a leading cause of breakdowns in medium and large electric motors [9].

When a rotor experiences broken bars, it triggers several adverse effects on the machine, including increased vibrations, elevated noise levels, reduced efficiency, and overheating due to excessive current flow in the unaffected bars [10]. Furthermore, broken bars can disrupt torque, speed, and line current, leading to premature ageing of the machine [5], [10].

If the detection of a broken bar in a three-phase induction motor is delayed, the situation can worsen as additional bars break, potentially resulting in eccentricity faults or complete machine shutdown [9]. A single broken bar does not cause an immediate machine shutdown, but the electrical current distributed to the remaining bars can lead to further breakages, causing an imbalance in electromagnetic forces and localized overheating. This imbalance places significant mechanical stress on the components, accelerating wear on bearings and resulting in eccentricity faults. In severe cases, it can even lead to damaging contact between the rotor and stator, resulting in catastrophic consequences for the machine. Additionally, localized overheating can cause winding failures, ultimately necessitating a complete machine shutdown [6], [10]–[12].

Here are various techniques for detecting faults in electrical machines based on different fields of science and technology. These techniques include:

- Thermal monitoring [13]
- Vibration and noise analysis [14]

- Signal analysis such as supply voltage [15]
- Analysis of magnetic flux [16]
- Electrical current analysis as in the Motor Current Signature Analysis (MCSA) method [17]

The most commonly used technique for detecting broken bars is based on MCSA [18]. However, this technique has some problems, such as the emergence of components that identify the fault due to bearing failure, fluctuations in the supply voltage, or low-frequency torque oscillations. Therefore, the reliability of diagnostics made by analyzing the electrical current is questionable since they can also indicate false failures due to ventilation ducts in the machine [19].

Methods that use FBGs for measuring the dynamic deformation of the electromagnetic field have been successfully applied in three-phase induction motors for rotor fault identification [20]. However, the data analysis and signal processing require the use of the software after data collection and visualization of results in graphs for fault detection [20]. This approach can complicate the process and make it susceptible to human errors in visually analyzing the graphs, as well as create a dependency on being connected to a machine with the software to perform further analyses. Therefore, this work aims to present the instrumentation of a sensor that has good sensitivity to fault conditions in MIT rotors and an algorithm that can be used in the cloud without the need to analyze the signal in software.

1.2 Objective

1.2.1 General Objectives

The objective of the project is to develop and validate an algorithm in Python running in the cloud for an automatic fault detection system in TIMs rotors through the analysis of dynamic deformation measured by FBG.

1.2.2 Specific Objectives

- study the failures in TIMs
- study the causes and effects of the broken rotor bar in TIMs
- monitor the rotor failures by the dynamic deformation measured by FBG
- create and filter a database
- Verify the effectiveness of the algorithm in the analysis of the TIM.

1.3 Document Structure

This document is divided into six chapters. The first chapter presents the introduction to the topic, along with the general sections relevant to the paper and its objectives. The second chapter reviews the types of failures in the TIM and discusses methods for identifying broken bars in rotors and the dynamic deformation in induction motors. The third chapter provides the theoretical foundations related to all the subjects utilized in the research. The fourth chapter describes the methodology employed during the research process. The fifth chapter presents the results obtained through the applied methodology. Finally, the sixth chapter provides a summary of the paper's contributions and outlines future work.

Chapter 2

Literature Review

This chapter presents a state-of-the-art review of monitoring and fault detection methods in rotors of TIMs. Firstly, information is provided on the construction characteristics of a rotor and the motor itself. Next, the potential causes of failures in these components, as well as the main types of failures that can occur in rotors, are discussed. Then, the main existing techniques for identifying and diagnosing these failures are presented. Finally, the specific contributions of this work are detailed. Several studies have proposed different approaches to diagnose faults in three-phase induction motors, including broken rotor bars, eccentricity, misalignment, and mechanical imbalance.

2.1 Rotors Constructive Aspects

In induction motors, the rotor's magnetic circuit comprises steel laminations, which are typically the same type used in the construction of the stator. There are two main types of rotors: wound rotors and squirrel cage rotors, where wound rotors are built similarly to the stator, with the rotor windings connected to the power supply phases using a set of brushes and rings mounted on the rotor shaft [6].

Squirrel cage rotors utilized in induction motors are constructed with conductors composed of either copper or aluminium. Copper bars are commonly employed in high-power motors, while aluminium bars are favoured in low and medium-power motor applications.

These bars can be integrated into the rotor structure through two methods: casting within an aluminium alloy structure or incorporating pre-moulded copper bars. Short-circuit rings are employed at each end of the bars to facilitate electrical connections. In low and medium-power motors, aluminium rings are used, while high-power motors use copper rings [21]. Notably, these rotors typically lack insulation between the rotor bars and the magnetic circuit, as the low resistance of the aluminium alloy effectively prevents current flow through the magnetic laminations. However, current flow through the magnetic circuit in the rotor only occurs in the presence of broken bars [6].

The construction of wound rotors and squirrel cage rotors, as well as the arrangement of the bars and short-circuit rings, are illustrated in 2.1. These visuals would enhance the understanding of the rotor's construction and contribute to a more comprehensive analysis of the induction motor's operation.

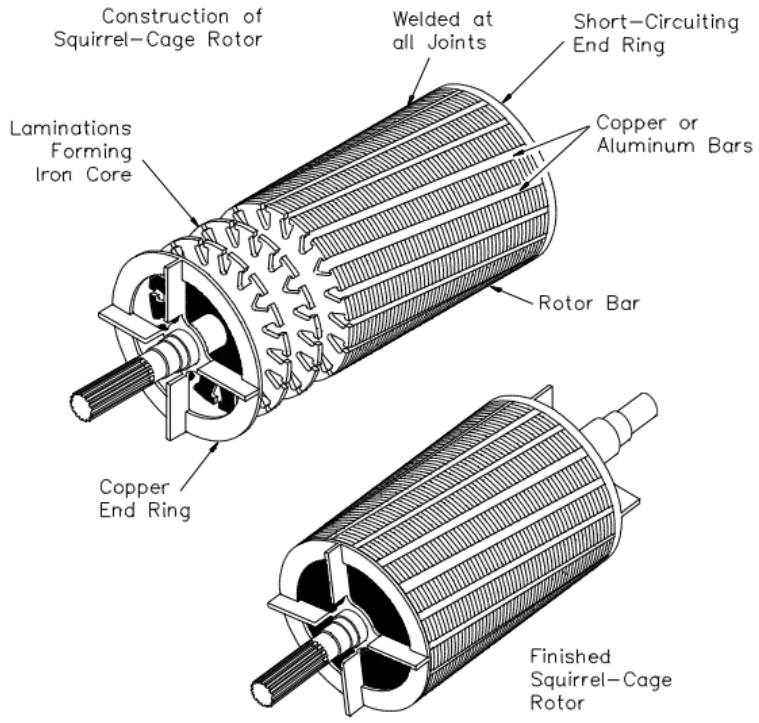

Figure 2.1: Cage rotor with its bars and short-circuit rings.
source: [22]

2.2 Faults Involving Rotors

Rotor bar faults account for approximately 10% of all failures that occur in electric motors in the industry [5]. Once the rotor bars are broken or cracked, they are rarely repairable, requiring the substitution of the rotor. These failures can arise due to various causes, including mechanical, magnetic, thermal, environmental, and residual stress factors. A rotor failure significantly exacerbates the excessive current flow in the adjacent bars when these parameters exceed the expected and allowable values, thereby significantly shortening the motor's lifespan. A rotor failure results in asymmetry [5], leading to reduced and varying torque as well as current imbalance [23].

2.2.1 Eccentricity Faults

Eccentricity failure occurs when there is an uneven air gap between the rotor and the stator. This imbalance of magnetic flux creates harmonic components in the current spectrum, which can be used to identify faults [10]. There are three types of eccentricity failure: mixed eccentricity, dynamic eccentricity, and static eccentricity. Figures 2.2 and 2.3 illustrate two representation of the types of eccentricity failure in an induction motor.

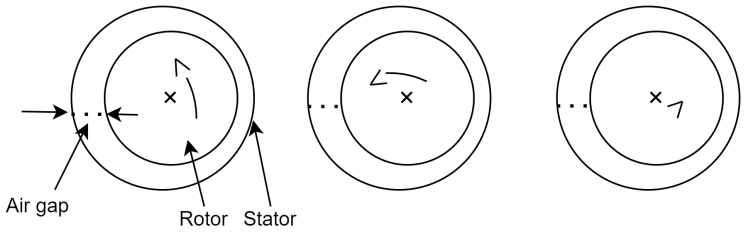

Figure 2.2: Schematic representation of static eccentricity faults in an induction motor. Source: adapted from [24]

Static eccentricity refers to a situation where the rotor's centre remains fixed but is consistently displaced from the centre of the stator. In contrast, dynamic eccentricity occurs when the centre of the rotor continuously shifts away from the centre of the stator, reaching the minimum air gap between them. Mixed eccentricity, the most common

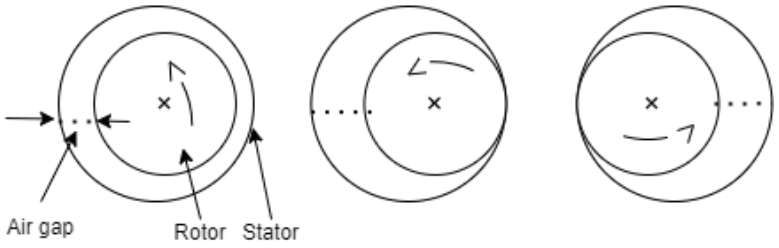

Figure 2.3: Schematic representation of mixed eccentricity faults in an induction motor. Source: adapted from [24]

type, arises when the geometric centres of rotation for both the rotor and stator do not align. This combination of dynamic and static eccentricities leads to variations in the magnetic flux of the machine due to the changing air gap, resulting in an imbalanced current flow that can be detected in the current spectrum. Diagnostic techniques for eccentricity faults primarily rely on current spectrum analysis, which distinguishes them from rotor bar failures. Compared to rotor bar failures, eccentricity faults are relatively straightforward to diagnose [6].

Eccentricity faults have numerous adverse effects on machine performance, including vibrations, accelerated bearing wear, increased losses, reduced efficiency, and elevated operating temperatures. If left uncorrected, eccentricity faults can lead to catastrophic damage, such as rotor-stator contact, ultimately resulting in core and stator winding destruction [24].

2.2.2 Rotor Broken Bar and Short-Circuited Ring Breakages

Squirrel cage rotors commonly experience two types of faults: broken bars and short-circuit ring faults and These faults can impact the performance of induction motors [10]. Figure 2.4 provides a visual representation of these fault types for better understanding and identification. Detecting and promptly addressing these faults through regular inspections, monitoring techniques, and advanced diagnostic tools, also will reduce maintenance requirements and costs, and is crucial to ensure the reliable operation and longevity of squirrel cage rotors.

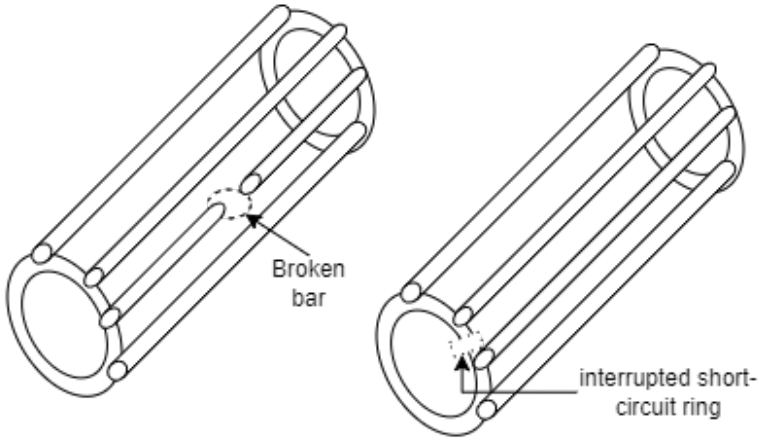

Figure 2.4: Broken bar fault and interrupted short-circuit ring in a squirrel cage rotor. Source: adapted from [6]

Several factors can lead to failures in broken bars and short-circuit rings in squirrel cage rotor induction motors [6], [24]. These factors include:

- Thermal stress is caused by overloads, imbalances, excessive material losses, or sparks, especially in fabricated-type rotors.
- Magnetic stress resulting from electromagnetic forces, magnetic unbalance pull (UMP), magnetic noise, or vibrations.
- Residual stress due to manufacturing issues.
- Dynamic stresses caused by shaft torques, centrifugal forces, or cyclic stresses.
- Environmental stresses such as contamination or material abrasion from chemicals or humidity.
- Manufacturing problems like air bubbles in the material or poorly made welds, result in sections of high electrical resistance in the bars or short-circuit rings.
- Mechanical stress is caused by fatigue in components, bearing wear, delamination of the magnetic core, and other factors.

When a fault happens in the rotor of a TIM, it introduces an imbalance in the rotor's structure, leading to various effects on the machine's performance. One significant consequence is the imbalance in line currents, causing fluctuations and a decrease in the average torque output [10]. These effects become more pronounced in machines operating with high inertia, where oscillations are noticeable in line currents and electromagnetic torque. In contrast, machines with low inertia exhibit more prominent oscillations in mechanical speed and stator current amplitudes[6].

Despite the presence of a broken bar, the machine does not shut down immediately. The electrical current that would flow through the broken bar is redistributed to adjacent bars. However, this redistribution leads to increased overload and excessive heating, which can eventually result in failures in additional bars. If a significant number of bars break, it may ultimately lead to machine shutdown. It's important to note that the electrical stress caused by a broken bar failure intensifies exponentially as more bars break, diminishing the machine's overall lifespan and potentially necessitating its shutdown [6], [10].

2.3 Techniques to Identify Rotor Bar Faults

2.3.1 External Noise Measurement

The external noise analyzed in the frequency spectrum using FFT is proposed by [25] to diagnose broken bars. The authors use a hybrid system of acoustic measurement with MCSA. Through psychoacoustic processing based on statistical models of Gaussian mixtures, the authors report having obtained success rates better than 84% for 1 broken bar with the motor unloaded. However, the models were trained on a specific machine, under controlled laboratory conditions, and the algorithm needed to be trained for each new situation. Another negative aspect of using external noise as a source for broken bar analysis is the need for microphones to be close to the motor, as sensitivity depends on the position and distance of measurement. Considering the need for High-quality measurement, expensive microphones are necessary, as observed by [26]. The diversity of

motor geometries and the disadvantage of external noise interference make the method impractical for use in an industrial environment.

The acoustic method of noise monitoring has been more commonly used for monitoring mechanical failures, such as bearing or roller failures, mechanical imbalances, loose or unrigid bearing pedestals, and critical rotational resonances of the shaft [26].

2.3.2 Current Measurement

Through the utilization of Motor Current Signature Analysis (MCSA) and the analysis of the spectral components of the stator current, fault-related information can be extracted, allowing for the effective identification and diagnosis of faults in induction motors. The application of Fast Fourier Transform (FFT) facilitates efficient and reliable signal processing, thereby enhancing the detection of unbalanced and broken rotor bar faults. An advantageous aspect of MCSA is its non-intrusive nature, requiring minimal additional equipment and offering valuable insights into the motor's condition and performance. However, it is important to note that there are certain limitations associated with MCSA. For instance, the stator current data should be sampled after the motor speed reaches a steady state, and the presence of noise in the current signal can pose challenges in signal analysis [17].

In the field of induction motor diagnosis, MCSA has been widely employed to detect faults related to unbalanced motor supply voltage and broken rotor bars. These faults, characterized by unsymmetrical supply and broken bars, can significantly impact the motor's operation. Various mitigation methods have been proposed to address the consequences of unbalance, with one of the simplest solutions involving the installation of overload protection and control circuits [17]. MCSA stands out as a straightforward and accurate technique, primarily relying on the measurement of stator current. However, it is essential to acknowledge that certain drawbacks exist.

2.3.3 IAS Analysis

According to [27] the research findings support the effectiveness of monitoring the IAS in detecting and diagnosing broken rotor bar faults in squirrel-cage induction motors. Simulation and experimental results have shown strong agreement, validating the practical application of IAS under similar operating conditions. Notably, IAS offers distinct advantages over current signature analysis, such as the ability to extract multiple features in both the time and frequency domains. The presence of modulating contours in the time domain and pole pass speed components in the frequency domain provide valuable information for identifying bar faults.

However, it is important to acknowledge some limitations and challenges associated with IAS. One drawback is the requirement for additional instrumentation and sensors, which may increase the complexity and cost of implementing IAS-based monitoring systems. Moreover, interpreting the IAS features requires expertise and careful analysis, as the presence of sideband components and contour modulations can be influenced by various factors, including motor load conditions and system dynamics. Additionally, the effectiveness of IAS may be limited in cases where other concurrent faults or anomalies in the motor are present, making it necessary to combine IAS with complementary fault detection techniques.

2.3.4 Temperature Analysis

Several temperature-based fault detection techniques have been proposed for identifying rotor faults in induction machines. These techniques rely on the analysis of temperature variations in different regions of the rotor. By measuring the temperature at multiple points along the rotor, it is possible to detect localized hotspots that indicate the presence of faults. Additionally, thermal imaging techniques using infrared cameras have been employed to visualize and analyze the temperature distribution in the rotor. These techniques provide valuable insights into heat dissipation patterns and can help identify specific fault signatures [28].

By monitoring temperature variations, it is possible to identify and diagnose various types of faults, including broken rotor bars and short-circuited rings. The use of temperature-based fault detection techniques, backed by case studies and experimental validations, has demonstrated promising results in enhancing the reliability and performance of induction machines. However, the fluctuation of environmental temperatures can adversely impact the accuracy of these techniques, making their application in industrial settings challenging [28].

2.3.5 Vibration Analysis with Acelerometers

The analysis of vibration levels in electrical machines is one of the techniques employed for the predictive identification of faults. Vibration parameters serve as indicators of how the motor was designed, assembled, installed, maintained, and operated. Every machine exhibits inherent levels of noise and vibration associated with its components. However, a range of vibration limits can be attributed to potential defects that compromise the equipment's performance. Increased vibration levels reflect the worsening of these defects [28].

In practice, accelerometers are used to measure vibration and obtain data. They belong to a class of transducers whose response is proportional to the acceleration experienced at the sensor's base. By utilizing mathematical derivation techniques, acceleration data can be converted into velocity and displacement variables. Vibration level data is typically acquired by sensors in the time domain and subsequently transformed into the frequency domain using Fast Fourier Transform in specialized software [28].

As stated by [29], the utilization of a biaxial optical accelerometer in induction motors enables the simultaneous measurement of acceleration and rotation in two perpendicular directions. This cost-effective solution proves valuable for vibration monitoring in electric machines, allowing for the detection of various faults, particularly rotor bar faults. However, it should be noted that the implementation of this technology may require a larger spatial arrangement due to the size and materials utilized for accurate measurement.

2.3.6 Dynamic Deformation Analysis Measured by FBG

Currently, a new method for monitoring rotors has been employed through the implementation of biaxial optical fibre accelerometers for vibration measurement using FBG (Fiber Bragg Grating) technology. The initial proposal was described in [29], where FBGs were used for rotor fault diagnosis. The authors fixed four sensors on a rigid rectangular support, positioned in opposite directions at different parts of the stator, to assess their influence on fault diagnosis. The results demonstrated that FBG sensors can be used for rotor fault diagnosis by analyzing dynamic deformation, as they are capable of detecting the characteristic fault frequencies in rotors.

In [30], the objective was to analyze the application of sensors as close as possible to the monitored rotor. Two FBGs, phased with a 120-degree separation, were bonded to the stator of the motor using adhesive. By applying small loads to the shaft, it was possible to detect the presence of characteristic frequencies through the measurement of the dynamic deformation of the stator.

In [20], the detection of faults in TIMs bearings was presented using dynamic deformation measurement with FBG-encased optical fibres installed in the motor stator. In this study, tests were conducted with the TIM operating under full load conditions, both with healthy and faulty rotors. The signals of dynamic deformation were analyzed in the frequency domain using FFT (Fast Fourier Transform). The spectra of the fault-free rotor exhibited prominent peaks related to the motor's power supply frequency and mechanical speed. Conversely, the spectra of faulty rotors showed additional frequency components associated with broken bar faults, with the main components being 30Hz and 120Hz. This study demonstrates the potential of FBG technology for monitoring the dynamic deformation of rotors in TIMs.

2.3.7 Analysis of Dynamic Deformation Measured by FBG

Recently, a new analysis method for electric machine rotors has been employed. For instance, the determination of temperature dynamics in a three-phase induction motor

using fibre optic Bragg grating sensors [31], and the detection of dynamic eccentricity in induction motors using fibre optic Bragg grating strain sensors [30].

The main objective of [30] is to test and analyze the dynamic strain measurement method in a no-load operation using fibre optic sensors. The mechanical and electrical forces are measured using a fibre Bragg grating (FBG), which is installed inside the motor, specifically between the stator teeth. The obtained measurements are then subjected to FFT analysis to identify the harmonic components present in the spectrum. On the other hand, [20] analyzed machines with and without faults, both under-loaded and no-load conditions. The aim was to provide experimental evidence regarding the reliability of rotor fault detection using FBG sensors through visual graphical analysis.

2.3.8 Time Domain Techniques

Time domain analysis refers to the examination of physical signals, mathematical functions, or time series data about it. It involves analyzing the values of signals or functions at different discrete occurrences, either in discrete or continuous time. Various characteristics can be extracted from the raw data, including mean, variance, Root Mean Square (RMS), standard deviation, peak-to-peak factor, skewness, and kurtosis. These features are calculated by segmenting the complete vibration data into one-second windows. Each feature is then calculated for each window within the entire eighteen-second vibration signal. Finally, all the extracted features are combined into a single file, providing a comprehensive representation of the time-domain features of the raw vibration signal [32].

2.3.9 Frequency Domain Techniques

Frequency domain techniques involve collecting the signal throughout time and processing it using the signal processing tool called Fast Fourier Transform (FFT). The FFT is a fast version of the Fourier Transform (FT) and allows the visualization of a time-domain signal in the frequency domain, enabling the identification and monitoring of fault evolution through its spectral components.

2.4 Contributions

As mentioned, TIM rotors can be monitored using various types of sensors, which measure different parameters such as vibration, temperature, electrical current, and acoustic emissions. These parameters can be analyzed in the time domain and frequency domain [10]. Due to being the third most common type of failure in induction motors, these techniques have been investigated for many years, and the advantages and disadvantages of each approach are well-known in the literature [6]. This study aims to analyze the dynamic strain measurement of TIMs to diagnose rotor failures. The failure is artificially introduced into the rotor to simulate wear or stress-induced cracks.

Recent studies have focused on implementing algorithms to optimize rotor fault diagnosis. However, no published study to date has addressed the use of FBG in combination with a cloud-based algorithm, replacing the catmaneasy software for fault detection in TIM rotors. Hence, another contribution of this work is to analyze the performance of the algorithm and explore the potential for fully replacing the catmaneasy software with a cloud-based algorithm, enabling data collection, analysis, and reporting from any location in an open manner. The dynamic strain signals of the motor will be analyzed in the frequency domain using an algorithm in Python that calculates by mathematical functions the principal components in the spectrum and then make the diagnoses of the rotor bar fault.

Chapter 3

Theoretical Rationale

In this chapter, we will provide a concise overview of the fundamental concepts to facilitate the understanding of the dissertation. We will cover concepts related to the characteristic frequencies of rotor faults and the theoretical foundation of Fiber Bragg Gratings FBG. Additionally, we will explain the working principle of the algorithm.

3.1 Effects of Rotor Broken Bar Fault on Different Engine Signals

In a healthy motor, balanced three-phase currents produce a rotating magnetic field in the air gap with a speed matching its synchronous angular velocity, w_s. This field induces an electrical current in the rotor bars, with a frequency proportional to the slip, s. The induced current generates another magnetic field in the rotor, aligned with its rotation and with an angular velocity of sw_s. The slip, represented by s, measures the percentage difference between the rotor angular velocity, w_r, and the synchronous angular velocity, w_s, and can be calculated using Equation 3.1:

$$s = \frac{w_s - w_r}{w_s}. \tag{3.1}$$

Understanding the slip and the relationship to the dynamics magnetic field is crucial

for analyzing induction motor performance. Monitoring slip helps identify deviations from ideal operating conditions and potential faults in the rotor. This knowledge enables effective diagnostic techniques and ensures reliable and efficient motor operation in various industrial applications.

Image a) in Figure 3.1 illustrates the operational diagram of a healthy motor, where $w_s = 2\pi f/p$ denotes the synchronous angular velocity, $w_r = w_s(1-s)$ represents the rotor angular velocity, $w_{slp} = w_s - w_r = sw_s$ represents the angular velocity of the slip, f represents the power source frequency, and p represents the number of poles in the machine.

In the presence of a broken rotor bar fault, asymmetries in the rotor result in the emergence of a counter-rotating magnetic field with the same magnitude but opposite direction. This counter-rotating field exhibits an angular velocity of $sw_s$when referenced to the rotor and an angular velocity of $(1-s)w_s - sw_s = (1-2s)w_s$ when referenced to the stator.

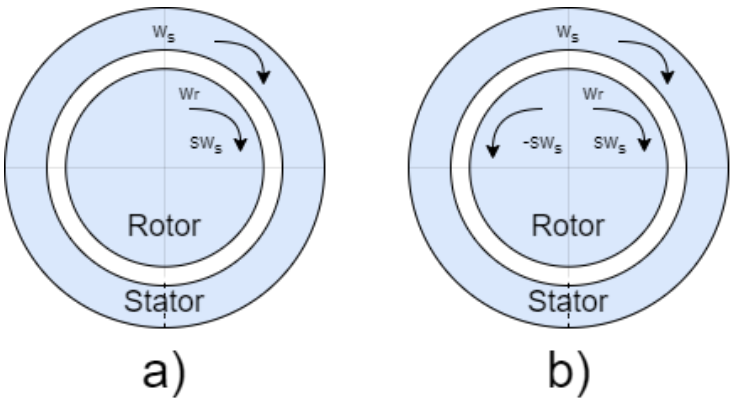

Figure 3.1: Operational diagram of a healthy motor, a) and with a broken rotor bar, b). Source: adapted from [16]

Image b) in Figure 3.1 depicts the operating scheme of an induction motor with a broken rotor bar fault. The asymmetric rotor produces a counter-rotating magnetic field, inducing an electrical current in the stator that characterizes the broken bar fault. This current has an angular velocity, w_bq, given by:

$$w_{bq} = w_r - sw_s = w_s(1 - 2s). \tag{3.2}$$

which results in the broken bar fault frequency, fbq, appearing in the external radial magnetic field and the line current:

$$f_{bq} = (1 - s)f - sf = (1 - 2s)f. \tag{3.3}$$

The interaction between the opposing rotating fields causes oscillations with a frequency of $2sf$ in the torque and motor speed. These oscillations act as frequency modulation on the machine's rotational frequency and all frequency components related to slip (s) [14]

In general, the frequency components that appear in the spectrum of the main machine signals are given by 3.2[14]:

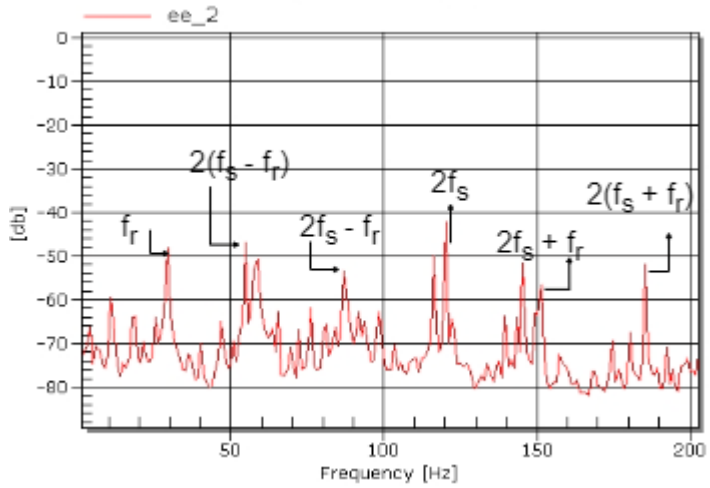

Figure 3.2: Stator strain frequency spectrum for the motor running at no load condition

The amplitudes of harmonic components in a motor system depend on three main factors: the load, the inertia of the motor-load assembly, and the severity of faults. Bellow it described the influence of each factor [33], [34]:

- Load: The amplitude of harmonics is directly related to the motor's operating load. Higher loads result in larger harmonic amplitudes, while lower loads lead to smaller

amplitudes.

- Inertia: The inertia of the motor-load assembly also affects the amplitudes of different frequency bands. When the inertia increases, the amplitude of the upper-frequency band decreases, but the amplitude of the lower-frequency band increases. On the contrary, reducing the inertia has the opposite effect.

- The severity of faults: The amplitudes of sidebands, which are additional frequency components, vary depending on the severity of faults in the motor. Factors such as the number and location of broken bars in the motor and whether the bars are completely broken or cracked directly impact the amplitudes of the sidebands.

Furthermore, it is important to highlight that under normal operating conditions, the amplitude of the upper-frequency band is typically greater than that of the lower-frequency band. However, this pattern is subject to change when the inertia of the motor-load assembly reaches or surpasses fifteen times the motor's inertia. In such cases, the amplitude relationship between the upper and lower frequency bands may be altered, potentially resulting in different harmonic behaviour in the motor system. This phenomenon warrants close attention as it can have implications for the overall performance and stability of the motor system under certain operating conditions.[33], [34].

When a broken bar exists in the rotor of the motor, it induces oscillations in the machine's speed at a frequency of $2sf$. These oscillations modulate the rotation frequency, f_r, resulting in the appearance of sidebands around fr in the spectrum. The sidebands can be identified by values of $fr\pm\ 2ksf$, and their magnitudes depend on the extent of speed oscillations and the asymmetry of the rotor.

To detect a broken bar fault, it is recommended to analyze the frequency range surrounding the motor's rotation frequency in the spectrum. By examining the presence and magnitude of frequency components expressed as fbq in the following equation:

$$f_bq = f_r \pm 2ksf. \tag{3.4}$$

Among the frequency components provided by equation 3.4 and shown in Figure 3.3, those with frequencies of $fr \pm 2sf$ exhibit the highest magnitudes. When $k = 1$, observing these frequency components enables more accurate identification of the rotor fault.

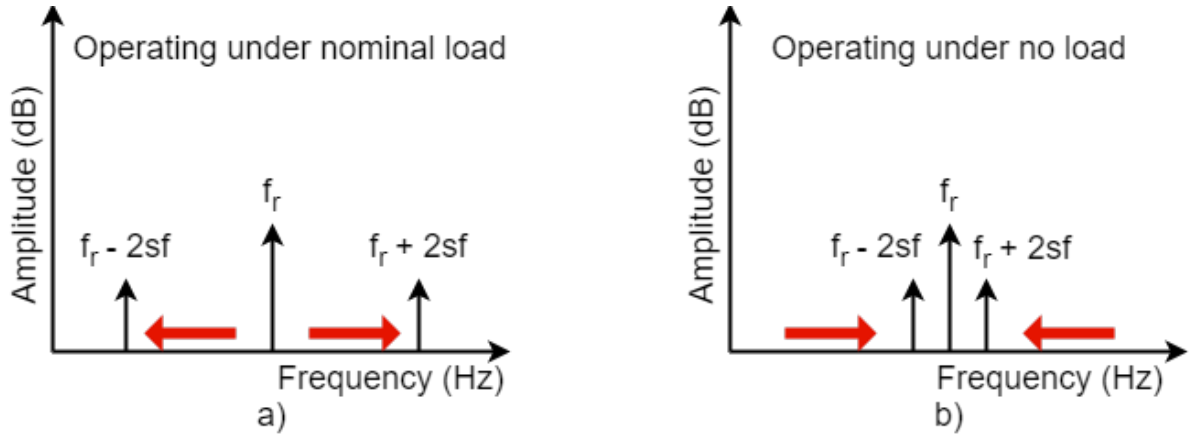

Figure 3.3: Position of the Sidebands Around the Mechanical Rotational Component

The twice-the-power supply frequency component holds significant importance in the vibration spectrum of an induction motor. This frequency emerges due to the peak attractive force between the stator and rotor of the machine when the rotor's magnetizing current reaches its maximum positive or negative value. Consequently, at each positive or negative peak of the power supply, the attraction force between the rotor and stator intensifies.

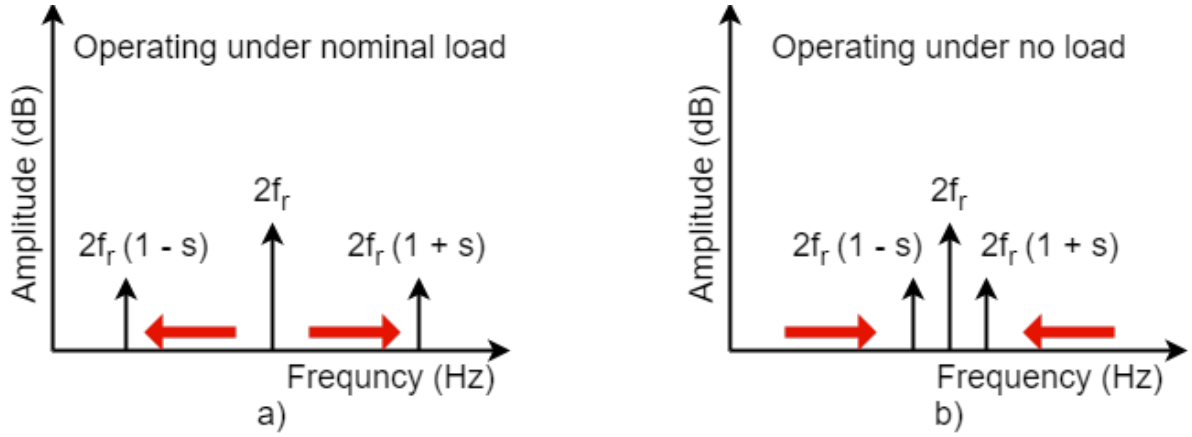

Figure 3.4: Position of the Sidebands Around Twice the Frequency Supply Component

The relative position of sidebands originated in the spectrum of a rotor broken bar for the region around its rotation frequency f_r, for $k = 1$, when: a) is the motor operating at rated load and b) image is the motor operating at no-load.

3.2 Fiber Bragg gratings in optical fibres

The utilization of optical fibres as sensors has witnessed substantial advancement since the groundbreaking discovery of their photosensitivity [35]. This pivotal finding paved the way for the creation of a novel category of fibre devices called Bragg gratings in optical fibres. Photosensitivity in optical fibres refers to the remarkable capability of modifying the refractive index of the fibre core by subjecting it to particular wavelengths and intensities of light, a process intricately linked to the core material properties. This capability has opened up exciting possibilities for developing highly sensitive and versatile optical fibre sensors with a wide range of applications in various fields[36].

Uniform fibre Bragg gratings (FBGs) are structures characterized by a periodic sinusoidal modulation of the refractive index in the photosensitive fibre core, with an effective refractive index denoted as n_{eff}. This modulation occurs perpendicular to the longitudinal axis of the fibre, with a constant period Λ. The refractive index modulation is achieved by subjecting the photosensitive core to an intense interference pattern, resulting in parallel planes with varying refractive index amplitudes perpendicular to the longitudinal axis [35], [36].

This modulation acts as a reflective spectral filter, selectively reflecting a narrow band of wavelengths that satisfy the Bragg condition [35]–[37]. The Bragg wavelength λ_b is determined by the equation:

$$\lambda_b = 2\Lambda n_{eff}. \tag{3.5}$$

The principle of operation is based on the interaction between the propagating light mode within the fibre and the periodically changing refractive index. Each plane of

the grating scatters the confined light within the fibre, and when the Bragg condition is met, the contributions from each plane interfere constructively in the counter-propagating direction. This results in a reflection band with a central wavelength determined by the grating parameters. Conversely, if the condition is not met, the reflected light from each subsequent plane gradually becomes out of phase, leading to the attenuation of the reflected light intensity [36].

Figure 3.5 illustrates an FBG with a specific period Λ and shows the corresponding reflection and transmission spectra. When a broadband light source is coupled to the fibre, a portion of the light near the Bragg wavelength of the FBG is reflected, forming the incident spectrum. The reflected spectrum exhibits characteristics similar to those of a selective bandpass filter, while the transmitted spectrum represents the difference between the incident and reflected spectra, resembling a reject-band filter.

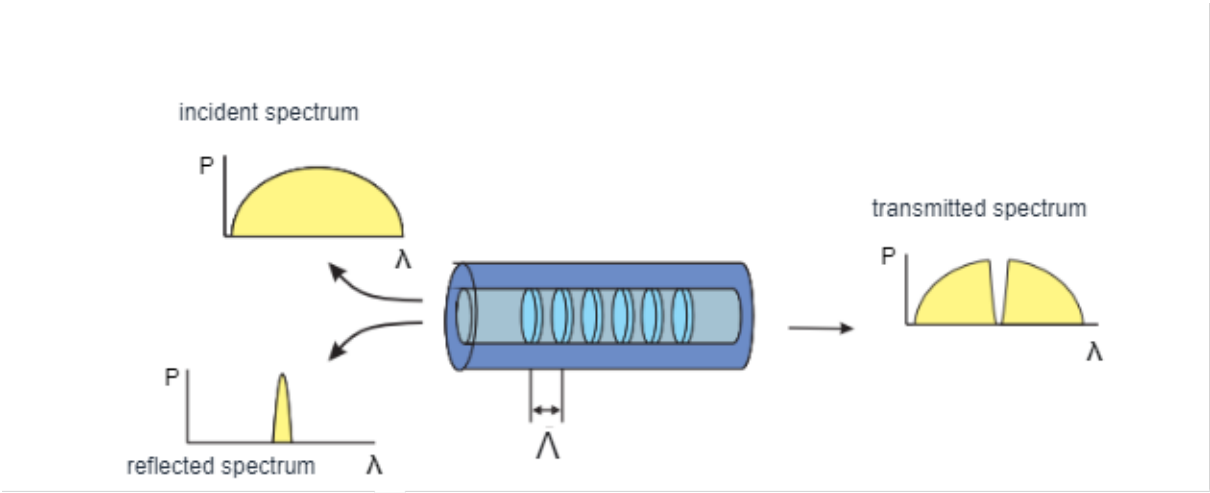

Figure 3.5: Schematic representation of static eccentricity faults in an induction motor. Source: adapted from [38]

The spectral response of FBGs can be customized by controlling parameters such as the grating period, length, and refractive index modulation amplitude. This flexibility enables the creation of FBGs with specific characteristics tailored for various applications, including wavelength filtering, dispersion compensation, and sensing.

Fiber Bragg Gratings (Fiber Bragg Gratings) offer several advantages, making them

highly desirable for sensing applications. One of their key strengths lies in their ability to accommodate multiple FBG sensors within a single optical fibre. This unique characteristic allows each sensor to be finely tuned to detect various quantities such as deformation, temperature, vibration, pressure, and displacement, among others [39]. Consequently, FBG sensors can be described as multifunctional devices.

The multiplexing capability of FBGs allows for the integration of multiple sensors into a single optical fibre through a process called wavelength division multiplexing WDM [39]–[42]. This multiplexing technique results in a cost-effective solution, as only one optical fibre and an optical interrogator are required to measure multiple points in an industrial environment. By utilizing a single fibre, it becomes possible to instrument multiple motors or detect various faults within these machines with minimal losses and no cross-interference between the different measured quantities [39]. This capability holds great promise for enhancing the efficiency and accuracy of industrial monitoring and control systems while significantly reducing overall implementation costs.

FBG provide a versatile platform with a wide range of applications in telecommunications, sensing, and optical signal processing. Their ability to selectively reflect or transmit light at specific wavelengths makes them essential components in modern optical systems. Ongoing research and development in this field are expected to drive advancements in fibre optic technology and unlock new possibilities for innovative applications.

3.2.1 Sensitivity of FBGs to Temperature and Deformation

The Bragg wavelength, as shown in equation (3.5), is dependent on the effective refractive index of the fibre core and the modulation period. These parameters can be influenced by external factors, leading to a shift ($\Delta\lambda_B$) in the Bragg wavelength value [36].

External disturbances in the environment, such as changes in temperature (ΔT) and strain (Δl) applied to the FBGs, cause variations in the Bragg wavelength. This can be expressed by (3.6) [36].

$$\Delta\lambda_B = 2\left(\Lambda\frac{\partial n_{eff}}{\partial l_{eff}} + n_{eff}\frac{\partial\Lambda}{\partial l_{eff}}\right)\Lambda\Delta l + 2\left(\Lambda\frac{\partial n_{eff}}{\partial T_{eff}} + n_{eff}\frac{\partial T_{eff}}{\partial\Lambda}\right)\Delta T. \tag{3.6}$$

The first term in (3.6) represents the effect of strain on the reflected Bragg wavelength. It accounts for changes in the grating periodicity and the photoelastic-induced alteration in the refractive index. This term can be described by equation 3.7, assuming negligible thermal effects [43].

The first term in Equation (3.6) represents the effect of strain on the reflected Bragg wavelength. It is related to changes in the grating periodicity and the photoelastic-induced alteration in the refractive index and can be represented by Equation (3.7) when thermal variations are negligible [43].

$$\Delta\lambda_B = \lambda_B(1 - p_e)\Delta\varepsilon. \tag{3.7}$$

In equation (3.7), $\Delta\varepsilon$ represents the relative strain per unit length, and pe is the photoelastic constant, defined as:

$$p_e = \frac{n_{eff}^2}{2}\left(p_{12} - v(p_{11} + p_{12})\right). \tag{3.8}$$

The relevant parameters for the photoelastic tensor components are $p11$, $p12$, and v. For a silica fibre core, these values are 0.113, 0.252, and 0.16, respectively. Using these parameters and $n_{eff} = 1.482$, equation (8) predicts a variation $\Delta\lambda_B = 1.2pm/\mu\epsilon$ [43].

Figure 3.6 visually demonstrates the effects of compression and tension on an FBG. Compression decreases the spatial period, causing the Bragg wavelength to shift towards shorter wavelengths. Conversely, tension increases the spatial period, resulting in a positive shift in the Bragg wavelength [38].

The second term in equation 3.6 represents the influence of temperature on the optical fibre. The shift in the Bragg wavelength is caused by thermal expansion, which alters the grating spacing and the refractive index. This shift, due to a temperature variation ΔT, can be expressed as (considering that the thermal expansion coefficient of the fibre

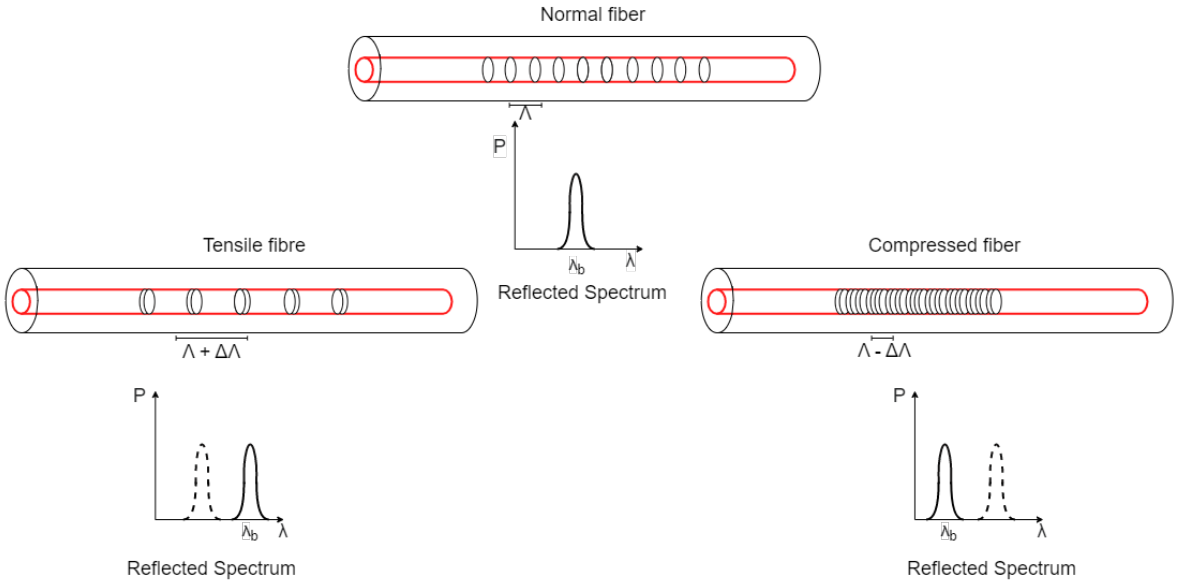

Figure 3.6: Spectral shift scheme of a Bragg grating network subjected to at rest, tension and compression.

Soucer: Adapted from [38]

is: $\alpha\Lambda = \frac{1}{\Lambda}\left(\frac{\partial\Lambda}{\partial T}\right)$.):

$$\Delta\lambda_B = \lambda_B(\alpha\Lambda + \alpha_n)\Delta T. \tag{3.9}$$

The thermo-optic coefficient for the fibre core of silica fibres is approximately $0.55 \times 10^{-6}\ ^{\circ}C^{-1}$. In the case of silica fibres doped with germanium, the thermo-optic coefficient α_n is typically around $8.6 \times 10^{-6}\ ^{\circ}C^{-1}$ [43].

.

Chapter 4

Implementation

This chapter presents the methodology used to obtain the experimental results. The methodology consists of several stages, as illustrated schematically in Figure 4.1. Firstly, the location of faults in the rotor is determined, followed by the collection of dynamic strain signals using an FBG installed in the TIM. These signals are then subjected to pre-processing and analyzed using classifiers to assess the power of each sideband component. Each of these steps will be described in detail in the subsequent sections.

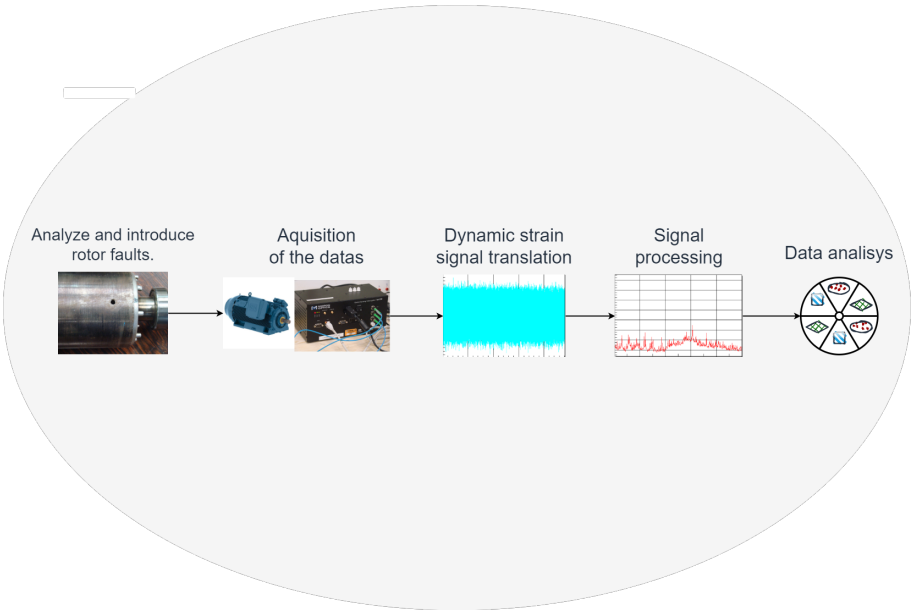

Figure 4.1: Diagram of the organization of the applied methodology

It is essential to consider that only this particular type of fault has been introduced and tested on the rotor. No tests involving other faulty rotors or more severe fault conditions, nor different types of faults, have been conducted.

4.1 Insertion of Rotor Fault

In this study, a fault was intentionally introduced into a TIM by creating a hole in one of the rotor bars using a drill and a bit. The faulty rotor was then installed in the TIM, while all other components remained in perfect condition. The purpose of this setup was to investigate the effects of the rotor fault on the motor's performance and to analyze the corresponding signals. Figure 4.2 provides a visual representation of the defective rotor used in the experimental tests.

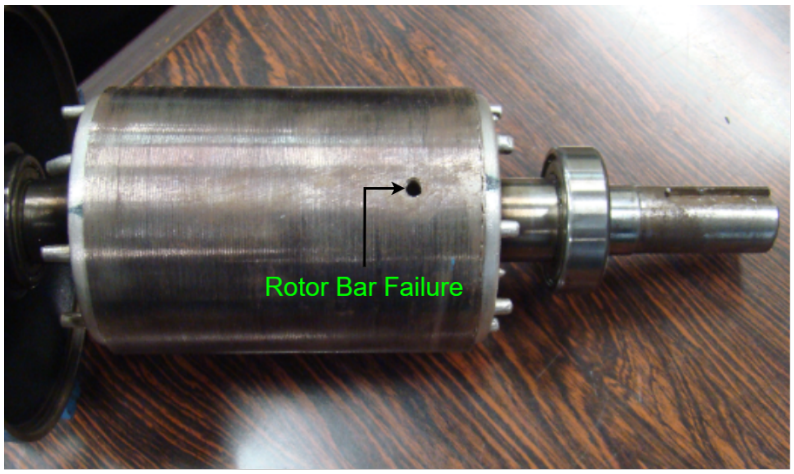

Figure 4.2: Rotor Fault

4.2 Experimental Arrangement

Figure 4.3 experimental setup employed in this study included a synchronous generator, a three-phase induction motor, an optical interrogator, and a resistive load. The motor under analysis was a Weg model FT80802, featuring 4 poles and a nominal power of 3 HP, connected in a $220V\Delta$ configuration. This setup enabled the collection of dynamic strain

data from the motor. To acquire the strain signals, an optical interrogator, specifically the SM125 model manufactured by Micronoptics, was utilized. The optical interrogator operated at a sampling rate of $1kHz$ with a resolution of $1pm$. The strain data were acquired using the CatmanEasy software provided by HBM and processed using a Python algorithm.

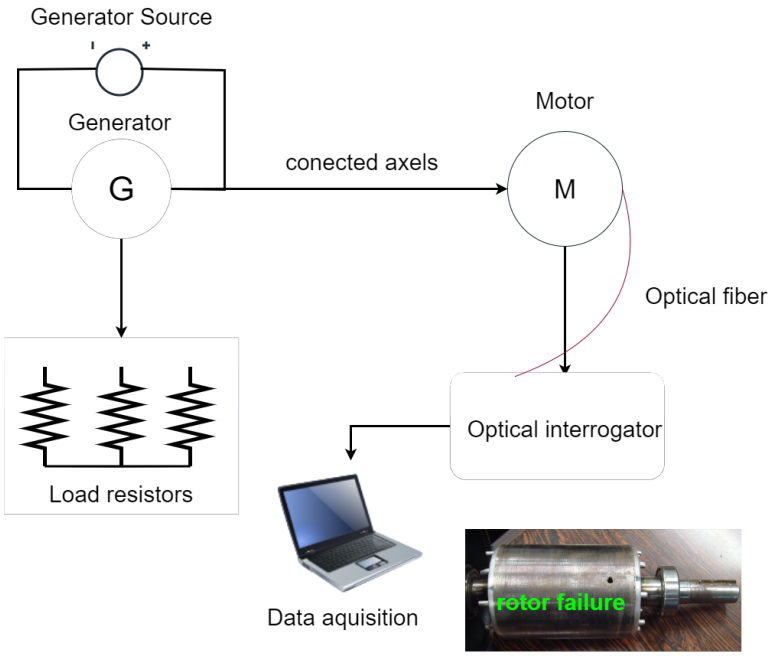

Figure 4.3: Experimental setup.

4.3 Installation of the FBG in the Motor Stator

In this study, the fabrication of the FBGs was conducted at the Photonics Laboratory of the Federal University of Technology - Parana. The FBGs were written on a single-mode optical fibre using a phase mask method with an Excimer laser operating at $248nm$ (Newport, Xantos). Four FBGs were successfully fabricated, each with a high reflectivity exceeding 70%. The Bragg wavelengths of the FBGs were carefully chosen at $1531nm, 1536nm, 1540nm, and 1560nm$, with a bandwidth of $0.3nm$. To ensure accurate strain measurements, the FBG strain sensors were pre-tractioned to achieve a *0.1 nm*

variation in the Bragg wavelength, enabling the detection of both positive and negative strains. The strain sensitivity for the FBGs is $1.2pm/\mu\varepsilon$.

To measure the dynamic strain, (FBGs) were used as sensors, they were installed symmetrically in the motor stator with a 90^{o} phase difference between each sensor. The installation of the deformation sensors on the motor stator involved a careful and systematic process. The following steps were followed to ensure proper bonding and alignment:

- The surface of the stator teeth was thoroughly cleaned using cotton soaked in acetone to remove any grease or contaminants. This cleaning process ensured a clean and suitable surface for bonding.

- The FBGs were positioned between consecutive stator teeth in a symmetrical and evenly spaced arrangement. This placement allowed for accurate strain measurement and analysis.

- Cyanoacrylate glue was applied to one end of each FBG, creating a small drop for bonding.

- Once the initial bonding was complete, the opposite end of each FBG was gently pulled with an estimated tension of $0.1nm$. A small drop of cyanoacrylate glue was then applied to this end, and the tension was maintained.

The installation process was repeated for the remaining three FBGs, following the same steps and maintaining a consistent approach throughout.

By following this meticulous installation process, the FBG deformation sensors were securely and accurately installed on the stator, allowing for precise strain measurement and analysis as illustrated in Figure 4.4

FBG need to be bonded to ensure they do not experience buckling and remain sensitive to both tensile and compressive mechanical forces. This is essential because, under compression, silica fibre is *23* times stronger than under tension [38]

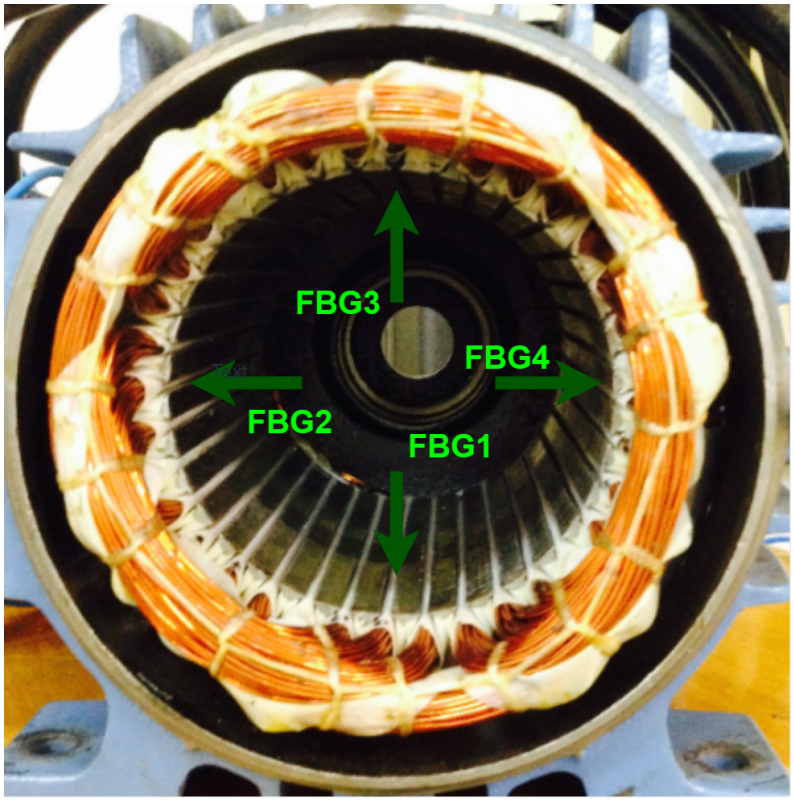

Figure 4.4: Photograph of the motor instrumented with four FBG sensors.

4.4 Experimental Setup

The setup involves the use of a synchronous generator to apply load to the induction motor. To accommodate load variation, the excitation voltage of the generator is adjusted accordingly, so a load cell is employed to accurately measure the load torque as illustrated in Figure 4.3

During the tests, the motors were operated in two different ways: one using the grid power supply and the other using a frequency inverter. Each motor was tested under three load conditions: no load, 75% load, and 100% load. In all tests, the motors were driven at a frequency of $60Hz$, which is commonly used in industrial environments. The purpose of these experiments was to simulate a normal operating environment as closely as possible, including factors such as noise, harmonics, and other disturbances. However, these conditions pose a greater challenge for fault diagnosis [3]

4.5 Creation of the Database

The database was constructed from the signals collected during the experimental tests, in which the motor operated with a faulty rotor, specifically a hole that was created in it. The dynamic strain signals of the motor were obtained through FBGs installed in the stator, and the following signals were collected and classified as follows:

- Grid supply with 75% load with the faulty rotor.
- Inverter supply with 75% load with the faulty rotor.
- Grid supply with 75% load with the healthy rotor.
- Grid supply with 100% load with the faulty rotor.
- Inverter supply with 100% load with the faulty rotor.
- Inverter supply with 100% load with the healthy rotor.

It's possible to observe the complete database used organized in Table 4.1

4.6 Pre-signals Processing

The operation of the FFT is based on the concept that it is possible to break down a signal into its fundamental sinusoidal components. Essentially, the FFT divides the signal into smaller segments, computes the Fourier Transforms of these segments, and then combines these transforms to obtain the final representation in the frequency domain. The Cooley-Tukey algorithm is one of the most well-known implementations of the FFT, which exploits the divisibility property of Fourier transforms to accelerate the process [44].

The data is collected in the time domain considering a sampling period of $1kHz$; however, to extract precise information about rotor faults, it is necessary to utilize the frequency domain. The signal transformation from the time domain to the frequency domain was performed using the FFT, implemented using the *numpy* library running on

the Google Colab platform. This transformation allows us to identify the PSD, which indicates the energy associated with specific frequencies that are indicative of rotor faults [45].

The resolution of the algorithm depends on both the size of the window, represented by *"fraction_split"* and the sampling rate, denoted as *"Fs"*. In the provided code, the sampling rate was set to 1000 Hz, while the window size, *"fraction_split"*, was defined as 2^{14}, which corresponds to $16,384$ data points [45]. Consequently, in this particular instance, the FFT resolution would be approximately 1000/16384, yielding a resolution of approximately 0.061 Hz. This signifies that the FFT can discern frequency components with an accuracy of approximately 0.061 Hz within the frequency spectrum. The determination of FFT resolution holds significance in the precise analysis of signals, particularly when examining closely spaced frequency components.

It is essential to operate with low resolution to enable the identification of significant power increases in the spectrum. Without sufficient resolution, it would be challenging to detect these abrupt changes in power. Taking into account the sampling period, the number of channels, sensors, and the database following filtering and transformation, the relationship of the workspace data is presented in 4.1

In the loop processing the fractionated data, we applied the unilateral FFT using a custom function called *"fft_unilateral"*. The unilateral transformation is useful when we are interested solely in the positive frequencies of the frequency spectrum, which is common in many practical applications. Subsequently, we applied a logarithmic transformation to enhance the visualization of results, as it accentuates the differences between frequency components and allows for a more intuitive interpretation.

The dynamic strain signals of the motor and the frequency spectra exhibit characteristic frequency values and behaviours that reflect the motor's operation, as well as the characteristic components of rotor faults. To ensure reliable fault detection, the obtained dataset was used to develop an algorithm in Python.

Setup	Channels	Number of readings	Database after FFT
COPEL Healthy 100%	8	91841	53
COPEL Fault 75%	8	197862	117
COPEL Fault 100%	8	240897	96
GENERATOR Healthy 100%	8	826404	403
GENERATOR Fault 75%	8	132198	64
GENERATOR Fault 100%	8	104267	50

Table 4.1: Database analyzed in the script

4.7 Algorithm Development

The data extraction process from the sensors involves two main steps. Firstly, the signal is collected from the optical interrogator using a notebook. Secondly, the collected data is opened and analyzed using the software's filtering and analysis mode to make necessary adjustments. The *apread* library (Catman AP Reader) facilitates the opening of raw files obtained from the optical interrogator within a virtual environment. This enables detailed analysis of the raw data and provides insights into the measurements. To carry out this external action, logical loops were implemented to achieve the opening and dissemination of all channels present in the collected data. For each trial state, there were 8 data collections conducted by the sensors in different channels. Consequently, all the collections were opened, segregated by trial type, appropriately grouped, and named. This was done in preparation for the subsequent FFT analysis, which allowed for the aggregation of results from the 8 distinct measurements for the same state.

The strategy employed for peak detection and data analysis involved several key steps. Firstly, we verified the correctness of the measurement to distinguish genuine signals from

noise or unexpected readings. Subsequently, we calculated the slip by identifying the main components, f_r and $2f$. Then, we proceeded to search for additional peaks alongside the main components. If two or more peaks aligned with the expected values, as reported in [20], and the average numbers matched our calculations, we could reasonably infer the presence of a rotor bar fault.

After analyzing this data, it is stored, and the script iterates through all the data sets generated by the FFT of each sample period, as explicitly explained in the signal processing chapter. Subsequently, a loop is established to perform this calculation logic for all data sets generated by the FFT of each segment. Averages are then calculated across all these data sets. With the computed power values and the frequency range in which the majority of samples are located in the frequency spectrum, it is characterized as either an identified fault or an unidentified fault.

The highest power peaks are expected to correspond to the components f_r and $2f$. Consequently, we estimate the maximum power in our dataset in decibels. Following this, a sweep is conducted using a maximum value command within a segment where we anticipate the presence of peaks indicating a fault. This allows us to determine the frequency associated with the maximum value within this interval. If this value significantly exceeds the average power of the surrounding adjacent data and falls within the expected frequency range, the loop identifies it as a peak. However, if it falls within the error margin of the adjacent peaks and no significant peaks are detected in the anticipated locations, it is classified as unidentified. Subsequently, after the loop has processed all the data for a given trial, it will provide a list of identified and unidentified peaks.

When any reading indicates high-power values at unexpected frequencies, the script automatically discards these readings as measurement faults. Due to the substantial volume of data, significant portions of this data often do not provide conclusive information due to reading errors and thus need to be filtered to ensure accurate diagnostics.

In this virtual environment, key components that can identify rotor faults are discernible. The analysis within this environment plays a crucial role in fault detection and allows for a deeper understanding of the data, aiding in the identification of rotor faults.

In Figure 4.5 it's possible to visualize the inputs of the data and the outputs.

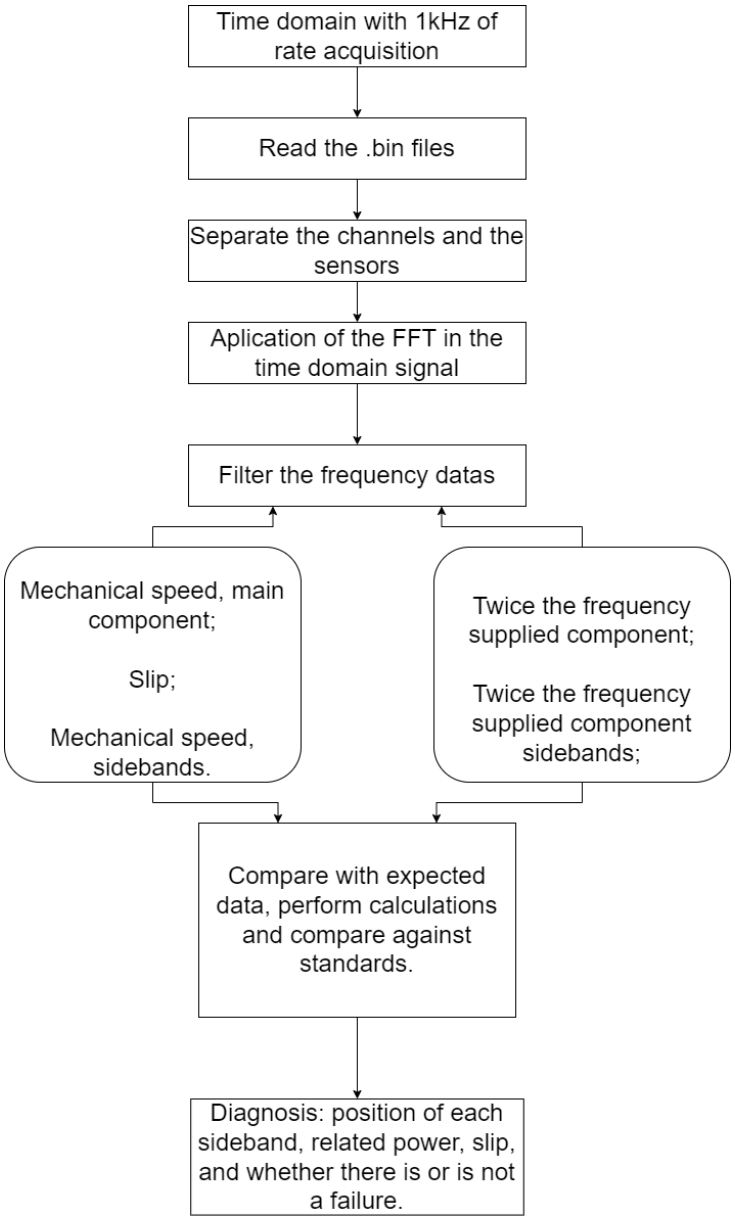

Figure 4.5: Input and Output Data Flow Diagram of the Algorithm.

Chapter 5

Results and Discussions

This chapter presents the key analytical results derived from information extracted from the dynamic deformation signals of the TIM using FBG sensors.

In the context of this study, the proposed approach was employed to replace the analytics method of HBM's CatmanEasy software and diagnose faults in TIM rotors. This was achieved by utilizing the Python programming language within a cloud-based system. The advantage of this approach lies in its ability to access and process collected files from the interrogator remotely, utilizing Google Colab tools. It enables data processing, analysis, and the classification of rotor health, all from a generic machine.

This paragraph describes the results obtained using an algorithm to analyze the signal extracted from the dynamic deformation signals of TIMs using FBG. The proposed approach was used for the detection of TIM rotor faults. The term "detection" refers to discovering the rotor fault by an algorithm. During operation, the motor experiences losses such as magnetic and Joule losses, leading to an increase in motor temperature. FBGs within the motor can detect this temperature rise [31]. However, the excitation due to temperature in the motor is greater than the excitation due to mechanical deformation. Therefore, when the signal measured by the FBG is analyzed in the frequency domain, the temperature increase in the motor does not interfere with the fault identification, Although this parameter also affects the value of λ_B.

5.1 Experiments Conducted with Load and Grid Power Supply

Figures 5.1, 5.2 and 5.3 illustrate the frequency spectra obtained for the TIM operating at a power supply frequency of 60 Hz with a rotor fault and a healthy one considering two different loads. For the two considered loads (operating with fault), the frequency spectra exhibit the same frequency components, related to mechanical and electromagnetic forces in the motor. The only differentiation among these spectra lies in their respective values of the sidebands frequencies and power. The value of these components is directly related to the rotational speed of the axis, which decreases as the load applied to the motor increases with failure and without it.

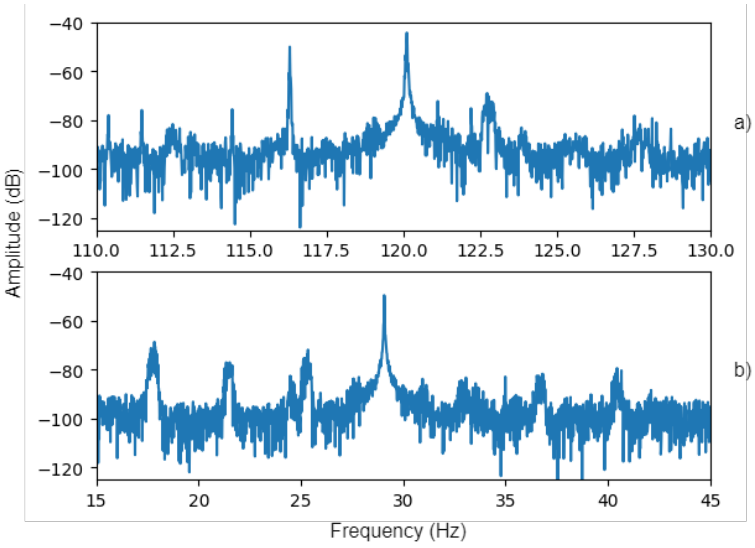

Figure 5.1: Stator strain frequency spectrum for the broken rotor bar near, twice the supply frequency, a) and the rotating frequency, b). The motor operates on a *60 Hz* grid and at *100%* load conditions.

Analysing the first dataset in Table 5.1 the motor is running with a healthy rotor and 100% of load with a slip $s = 4.85\%$ and it related with the main component desolated from the centre, 30 Hz, the second dataset is the rotor with a fault and operating at 75% of the nominal load with a slip $s = 1.52$ and the sideband in the two principal components, $f_r - 2f = 28.06\ Hz$, $f_r + sf = 31.014\ Hz$, $2(1-s)f = 118.455\ Hz$, $2(1+s)f = 123.942$

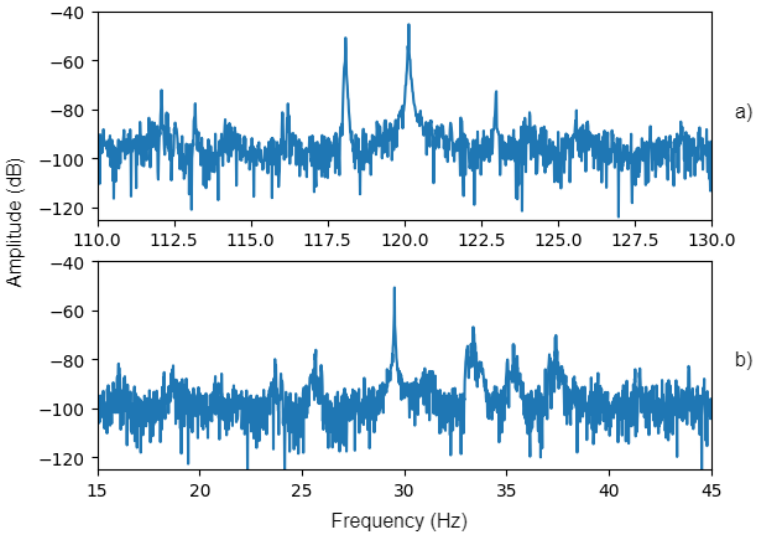

Figure 5.2: Stator strain frequency spectrum for the broken rotor bar near, twice the supply frequency, a) and the rotating frequency, b). The motor operates on a *60 Hz* grid and at *75%* load conditions.

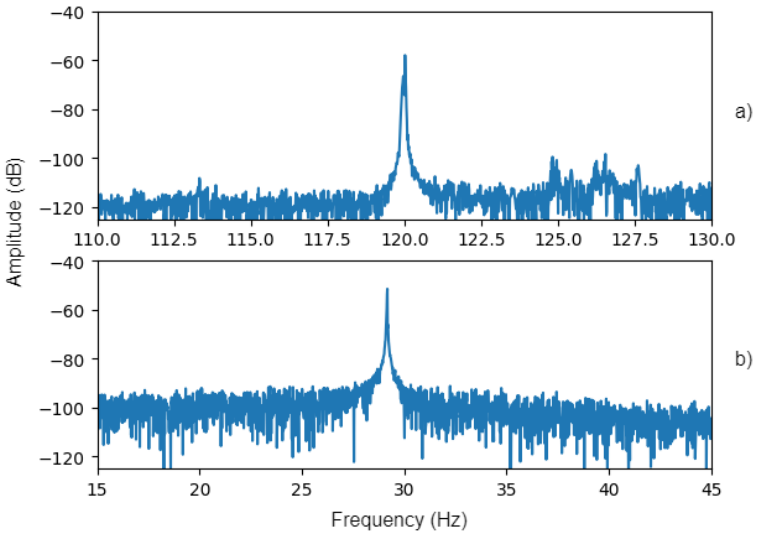

Figure 5.3: Stator strain frequency spectrum for the healthy rotor bar near twice the supply frequency, a) and the rotating frequency, b). The motor operates on a *60 Hz* grid and at *100%* load conditions.

Hz. the last one is the TIM operating with rotor fault at 100% of the nominal load with a slip $s = 3.157$,and the sideband in the two principal components, $f_r - 2f = 25.325$ *Hz,* $f_r + sf = 32.995$ *Hz,* $2(1-s)f = 117.237$ *Hz,* $2(1+s)f = 124.683$ *Hz.* It was considered all the FBGs strain sensors and all the data collected in the analysis, and comparing with the results presented in [20], that was observed and matched the diagnoses, considering that all the data were running.

Table 5.1 presents the frequency components present in each of the power spectra and the correlated sidebands shown in the Figures, considering the main components at 120 Hz and 30 Hz. And in Table 5.2 it's possible to observe the number of data that was disregarded. In the developed script, the discarded data consists of responses that do not align with the rotor's health state during the respective test. The methodology for this classification is elaborated upon in Chapter 4.

Dataset	Slip(%)	Principal component(Hz)	Sidebands(Hz)
Healthy 100%	2.750	29.175	-
	2.750	120.005	-
Fault 75%	1.520	29.541	31.014 - 28.060
	1.520	120.138	123.942 - 118.455
Fault 100%	3.157	29.070	32.995 - 25.325
	3.157	119.929	117.237 - 124.683

Table 5.1: Frequency components of the TIM related to faults and principal peaks were analyzed for the motor operating with a load supplied by the grid.

For the initial set of tests, where the grid was used as the power source, we analyzed 4 peaks using the developed algorithm. We identified the highest power peak within the

range expected by analytical calculations and excluded readings that appeared inconclusive due to data acquisition errors. The algorithm is designed to compile the extracted data directly and applies a filter to remove inconclusive data lacking peaks from the main components f_r and $2f$.

There were several failures when attempting to detect faults solely based on the power of the main components. Consequently, we relied on the presence of sidebands and verified their positioning to determine their veracity. With the data that the algorithm identified as peaks, we analyzed all readings considered correct and calculated an average with the peak values to determine if they fell within the margin of analytical verification.

Dataset	30Hz Component	120Hz Component
Healthy 100%	0	20
Fault 75%	1	12
Fault 100%	1	20

Table 5.2: Number of data discarded when the motor operates supplied by the grid.

The strain spectrum of the stator is strongly influenced by the electromagnetic forces acting on the machine. In turn, the region around 30 Hz is more susceptible to mechanical forces such as mechanical speed or load imbalance. Lower slip values cause the frequency components caused by broken bar failures to approach the fundamental frequencies, making it more challenging to identify the fault when the motor operates at low loads. The broken bar fault could be identified in both spectral regions analyzed under the two load-tested conditions.

5.2 Experiments Conducted Operating with Load and Supplied by a Generator

Figures 5.4, 5.5, and 5.6 present the frequency spectra of the TIM operating under different load conditions, in 60 Hz, with a focus on both rotor fault and healthy operation considering that the motor is supplied by a generator, not the grid. The frequency spectra for both load conditions (with fault) display similar frequency components associated with mechanical and electromagnetic forces in the motor. The main distinction between these spectra is the values of the sideband frequencies and power. These components are directly linked to the rotational speed of the motor's axis, which decreases as the applied load on the motor increases, regardless of the presence of a fault.

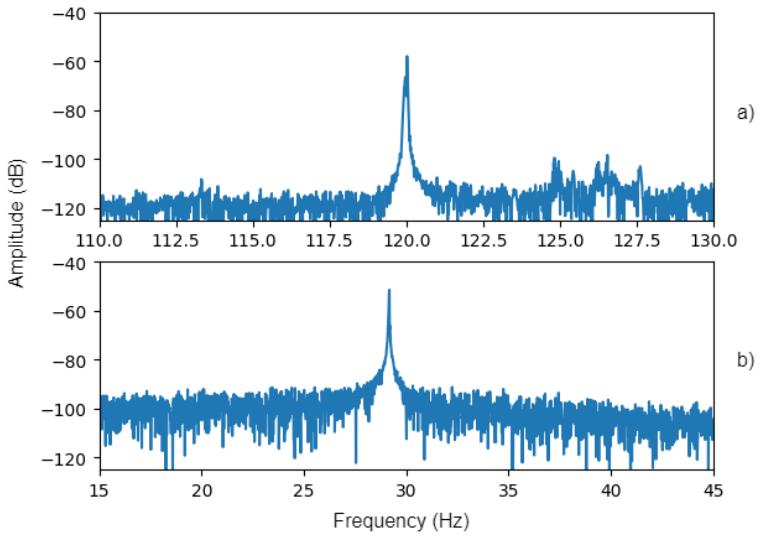

Figure 5.4: Stator strain frequency spectrum for the broken rotor near twice the supply frequency, a) and the rotating frequency, b). The motor operates on a *60 Hz* supplied by a generator and at *100%* load conditions.

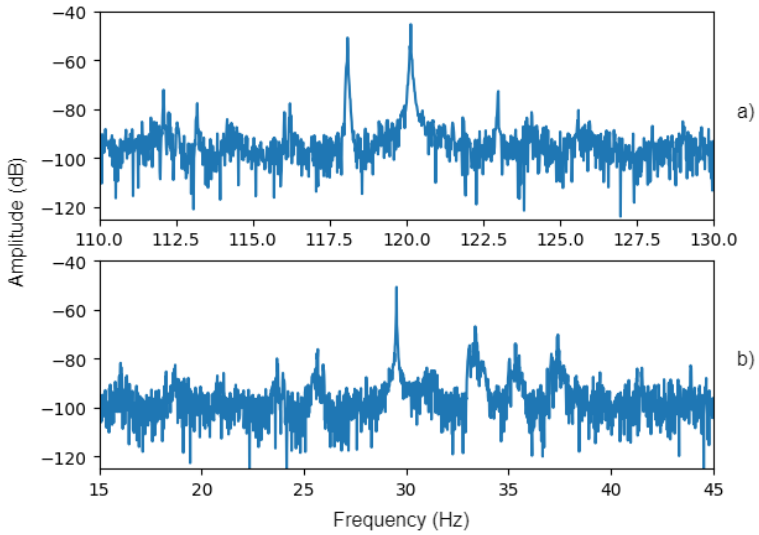

Figure 5.5: Stator strain frequency spectrum for the broken rotor bar near, twice the supply frequency, a) and the rotating frequency, b). The motor operates on a *60 Hz* supplied by a generator and at *75%* load conditions

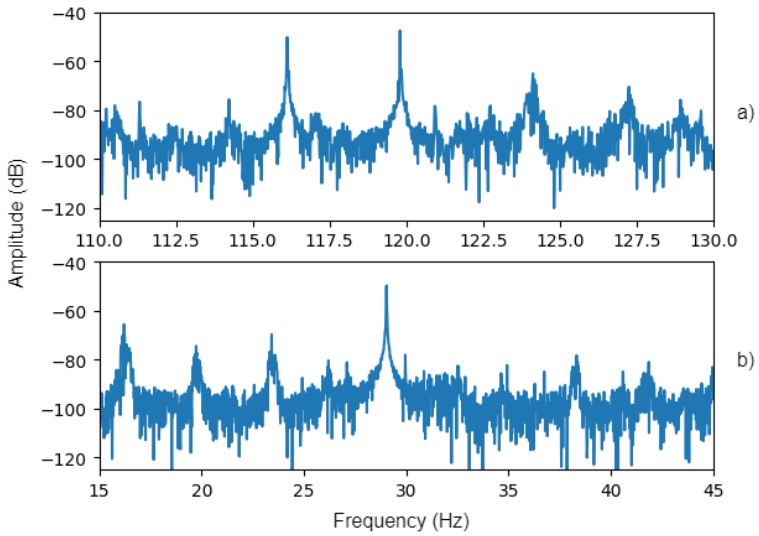

Figure 5.6: Stator strain frequency spectrum for the healthy rotor bar nea, twice the supply frequency, a) and the rotating frequency, b). The motor operates on a *60 Hz* supplied by a generator and at *100%* load conditions.

Analyzing the first dataset in Table 5.1, the motor is running with a healthy rotor and 100% of load with a slip of $s = 3.361\%$, and it is related to the main component deviated from the centre, $30Hz$. The second dataset represents the rotor with a fault operating

at 75% of the nominal load with a slip of $s = 0.513$, and the sidebands appear in the two principal components: $f_r - 2f = 28.6547Hz$, $f_r + sf = 29.04595Hz$, $2(1-s)f = 114.539Hz$, $2(1+s)f = 126.319Hz$. The last dataset represents the TIM operating with a rotor fault at 100% of the nominal load with a slip of $s = 3.16$, and the sidebands are observed in the two principal components: $f_r - 2f = 25.637Hz$, $f_r + sf = 32.4634Hz$, $2(1-s)f = 115.319Hz$, $2(1+s)f = 124.559Hz$. All FBG strain sensors and their collected data were considered in the analysis. Comparing with the results found in [20], it was observed that the diagnoses for the healthy rotor and the rotor fault operating at 100% load matched the expected results. However, the data from the rotor operating at 75% load with a rotor fault were more challenging to interpret. The sidebands from the *2f* component were clearly visible, but the positive one from the $30Hz$ component was harder to locate, probably due to the data not matching the expected spectrum.

In Table 5.3, we can find a detailed breakdown of the frequency components observed in each power spectrum depicted in the Figures. Specifically, the main components at 120Hz and 30Hz are highlighted. Additionally, Table 5.4 provides insights into the number of data points that were excluded during the analysis phase.

Dataset	Slip(%)	Principal component(Hz)	Sidebands(Hz)
Healthy 100%	3.361	28.992	-
	3.361	118.103	-
Fault 75%	0.513	29.846	28.655 - 29.046
	0.513	119.581	126.319 - 114.539
Fault 100%	3.160	29.053	32.463 - 25.637
	3.160	119.821	115.652 - 124.559

Table 5.3: Frequency components of the TIM related to faults and principal peaks were analyzed for the motor operating with a load supplied by the generator.

There were several inconclusive responses when attempting to detect the rotor fault using only the intensity and location of the main power components. Therefore, a verification of the positioning of the components f_r and $2f$ was developed to determine whether they were suitable averages or not, using Figure 5.3 as a reference. With the data that the algorithm identified as peaks, all the readings considered correct were analyzed, and an average was calculated with the peak values to assess whether it fell within the analytical verification margin. Those data discarded due to non-compatible reading are registered in the Tabel 5.2.

Dataset	*30 Hz* Component	*120 Hz* Component
Healthy 100%	2	6
Fault 75%	2	5
Fault 100%	4	12

Table 5.4: Number of data discarded when the motor operates supplied by a Generator.

The stator's strain spectrum is significantly affected by the electromagnetic forces exerted on the machine. Conversely, the region around 30 Hz is more sensitive to mechanical forces like mechanical speed or load imbalance. When the slip values are lower, the frequency components resulting from broken bar failures tend to get closer to the fundamental frequencies, making it more difficult to detect the fault under low load conditions. However, the broken bar fault could still be identified in both analyzed spectral regions for the two load-tested conditions.

5.3 Comparison of the Results in Both Setups

Considering the diagnosis provided by the algorithm, there were data points that were utilized to generate the average peak values, while others were discarded. Table 5.5 displays the data used, the rejected data, and the percentage of accuracy. The processing time for all data depends on the number of collected samples and the data acquisition time. In the presented study, the algorithm takes 39 seconds to complete data reading

and signal processing. The output includes responses related to the identified sidebands, mechanical rotation components, twice the power supply frequency component and the slip. Discarded data primarily consists of inconclusive readings. The accuracy percentage, Present in the fourth column of the table5.5, represents the proportion of all sample sets after performing FFT for which a conclusive diagnosis was possible and accurately reflected the test conditions.

Type	Samples discarded	Total simulations	Conversion rate (%)
COPEL Healthy 100%	20	53	62,264
COPEL Fault 75%	21	117	82,051
COPEL Fault 100%	13	96	86,458
GENERATOR Healthy 100%	8	403	98,015
GENERATOR Fault 75%	8	64	89,063
GENERATOR Fault 100%	8	50	68,000

Table 5.5: Rate and results of the algorithm

Chapter 6

Conclusions

In this study, broken rotor bars are detected using FBG strain sensors. The measurements are performed inside the motor and on the stator surface. The tests include one healthy rotor and one rotor with faults. Therefore, the results are not influenced by other mechanical parameters, such as motor assembly or vibration attenuation, as the air gap forces are transferred out of the TIM.

The motor was supplied by a power grid and by a generator and operated under 2 load conditions in both power supplies. The application of FBG for measuring the dynamic deformation of the TIM proved to be effective, regardless of the severity of the analyzed fault. It was observed that the main components at 120 Hz and 30 Hz played a crucial role in detecting rotor faults in the TIMs. The presence and positioning of these components were analyzed to determine the veracity of the fault detection. However, it was found that relying solely on the power of the main components led to several inconclusive responses. Therefore, the study highlights the importance of considering both the intensity and positioning of the main power components, as well as the presence of sidebands, in fault detection. Further research is needed to refine the analysis techniques and algorithms for accurately identifying rotor faults based on the frequencies present in the FBG sensor data.

The signal of dynamic deformation was pre-processed by the algorithm. The pre-processing involved using FFT and the APreader library to open and read the files. A

logical function was also used to apply another filter, ensuring that only signals containing relevant information for the analysis were considered, due to the fact that there are problems with the data acquisition by the sensors. The study concluded successfully, as all the filtering was accomplished, allowing the analysis and visualization of graphics with good resolution and shape if the user wants. It was possible to observe some differences between the values in the different supply modes, due to the speed variation caused by the grid fluctuations.

The results indicate that the algorithm is effective in detecting faults in the TIM rotor based on the motor's dynamic deformation, In both experiments. When utilizing grid-supplied power, we achieved an accuracy rate of $62,264\%$ for healthy motors, $82,051\%$ for faulty rotors at 75% load, and $86,458\%$ for faulty rotors at full load. Similarly, in the controlled-source experiment, we obtained an accuracy rate of $98,015\%$ for healthy motors, $89,063\%$ for faulty rotors at 75% load, and $68,000\%$ for faulty rotors at full load. One advantage of the instrumentation used in this study is its capability to replace the software catmaneasy for the analysis mode and it's important to highlight that a large number of samples were collected in order to have accurate measurements of strain signals. The development of the algorithm became crucial for the efficiency of data analysis, allowing it to process each test status in approximately 40 seconds. Recently, the implementation of algorithms for diagnosing rotor bar faults has become necessary, considering that most of the sensors used are affected by environmental vibrations, resulting in noisy signals. This complexity makes it challenging to verify the authenticity of the rotor status through scripts. Moreover, the presented instrumentation is non-invasive, as the motor cover, where the sensor is installed, can be easily removed.

The main contribution of this study is the novel application of an algorithm operating in a cloud platform, so it's possible to access from everywhere in different machines, and only with the data acquisition its possible to read the raw data and process them. those techniques optimized the detection of faults in TIM rotor measured by FBG. This work presents an innovative approach to fault detection in TIM rotors based on the motor's dynamic deformation, combined with a Python algorithm.

6.1 Future Papers

To continue the work presented in this paper, the following proposals are made:

- Analysis of combined faults, involving both bearing and rotor with different types of severity.
- Enhancement of the algorithm to make the data acquisition.
- Implementation of a trained network for statistical analysis, using other methods to identify the fault components in the spectrum.
- Development of sensor encapsulation for easy implementation.
- Develop an algorithm considering more loads applied.

Bibliography

[1] P. C. Krause, O. Wasynczuk, S. D. Sudhoff, and S. D. Pekarek, *Analysis of electric machinery and drive systems*. John Wiley & Sons, 2013, vol. 75.

[2] A. Siddique, G. Yadava, and B. Singh, "A review of stator fault monitoring techniques of induction motors," *IEEE transactions on energy conversion*, vol. 20, no. 1, pp. 106–114, 2005.

[3] M. R. Mehrjou, N. Mariun, M. H. Marhaban, and N. Misron, "Rotor fault condition monitoring techniques for squirrel-cage induction machine—a review," *Mechanical Systems and Signal Processing*, vol. 25, no. 8, pp. 2827–2848, 2011.

[4] T. Jokinen, V. Hrabovcova, and J. Pyrhonen, *Design of rotating electrical machines*. John Wiley & Sons, 2013.

[5] S. Nandi, H. A. Toliyat, and X. Li, "Condition monitoring and fault diagnosis of electrical motors—a review," *IEEE transactions on energy conversion*, vol. 20, no. 4, pp. 719–729, 2005.

[6] J.-C. Trigeassou, *Electrical machines diagnosis*. John Wiley & Sons, 2013.

[7] P. Zhang, Y. Du, T. G. Habetler, and B. Lu, "A survey of condition monitoring and protection methods for medium-voltage induction motors," *IEEE Transactions on Industry applications*, vol. 47, no. 1, pp. 34–46, 2010.

[8] R. Fiser and S. Ferkolj, "Application of a finite element method to predict damaged induction motor performance," *IEEE Transactions on Magnetics*, vol. 37, no. 5, pp. 3635–3639, 2001.

[9] A. Naha, A. K. Samanta, A. Routray, and A. K. Deb, "A method for detecting half-broken rotor bar in lightly loaded induction motors using current," *IEEE Transactions on Instrumentation and Measurement*, vol. 65, no. 7, pp. 1614–1625, 2016.

[10] H. A. Toliyat, S. Nandi, S. Choi, and H. Meshgin-Kelk, *Electric machines: modeling, condition monitoring, and fault diagnosis*. CRC press, 2012.

[11] R. Isermann, *Fault-diagnosis applications: model-based condition monitoring: actuators, drives, machinery, plants, sensors, and fault-tolerant systems*. Springer Science & Business Media, 2011.

[12] G. C. Stone, I. Culbert, E. A. Boulter, and H. Dhirani, *Electrical insulation for rotating machines: design, evaluation, aging, testing, and repair*. John Wiley & Sons, 2014, vol. 83.

[13] X. Ying, "Performance evaluation and thermal fields analysis of induction motor with broken rotor bars located at different relative positions," *IEEE Transactions on Magnetics*, vol. 46, no. 5, pp. 1243–1250, 2010.

[14] A. Sadoughi, M. Ebrahimi, M. Moalem, and S. Sadri, "Intelligent diagnosis of broken bars in induction motors based on new features in vibration spectrum," in *2007 ieee international symposium on diagnostics for electric machines, power electronics and drives*, IEEE, 2007, pp. 106–111.

[15] M. Nemec, V. Ambrozic, D. Nedeljkovic, and R. Fiser, "Detection of broken bars in induction motor through the analysis of voltage modulation," in *2006 IEEE International Symposium on Industrial Electronics*, IEEE, vol. 3, 2006, pp. 2450–2454.

[16] A. Ceban, R. Pusca, and R. Romary, "Eccentricity and broken rotor bars faults-effects on the external axial field," in *The XIX International Conference on Electrical Machines-ICEM 2010*, IEEE, 2010, pp. 1–6.

[17] K. S. Gaeid, H. W. Ping, M. Khalid, and A. L. Salih, "Fault diagnosis of induction motor using mcsa and fft," *Electrical and Electronic Engineering*, vol. 1, no. 2, pp. 85–92, 2011.

[18] J. A. Antonino-Daviu, M. Riera-Guasp, J. R. Folch, and M. P. M. Palomares, "Validation of a new method for the diagnosis of rotor bar failures via wavelet transform in industrial induction machines," *IEEE Transactions on Industry applications*, vol. 42, no. 4, pp. 990–996, 2006.

[19] M. Riera-Guasp, J. Pons-Llinares, F. Vedreno-Santos, J. A. Antonino-Daviu, and M. F. Cabanas, "Evaluation of the amplitudes of high-order fault related components in double bar faults," in *8th IEEE Symposium on Diagnostics for Electrical Machines, Power Electronics & Drives*, IEEE, 2011, pp. 307–315.

[20] K. M. Sousa, I. B. V. da Costa, E. S. Maciel, J. E. Rocha, C. Martelli, and J. C. C. da Silva, "Broken bar fault detection in induction motor by using optical fiber strain sensors," *IEEE Sensors Journal*, vol. 17, no. 12, pp. 3669–3676, 2017.

[21] I. Boldea, *Induction machines handbook*. CRC press, 2020.

[22] U. D. O. ENERGY, *DOE FUNDAMENTALS HANDBOOK*. ELECTRICAL SCIENCE. volume 4, 2016.

[23] J. Ilonen, J.-K. Kamarainen, T. Lindh, J. Ahola, H. Kalviainen, and J. Partanen, "Diagnosis tool for motor condition monitoring," *IEEE Transactions on Industry Applications*, vol. 41, no. 4, pp. 963–971, 2005.

[24] J. Faiz and S. Moosavi, "Eccentricity fault detection–from induction machines to dfig—a review," *Renewable and Sustainable Energy Reviews*, vol. 55, pp. 169–179, 2016.

[25] E. L. Miotto and A. Y. Nakano, "Análise de barras quebradas em rotor de motor de induçao trifásico por assinatura de corrente elétrica e por processamento psicoacústico," in *16o Simpósio Brasileiro de Micro-ondas e Optoeletrônica (SBMO) e 11o Congresso Brasileiro de Eletromagnetismo (CBMag). Momag*, 2014.

[26] M. Janda, O. Vitek, and M. Skalka, "Noise diagnostic of induction machine," in *The XIX International Conference on Electrical Machines-ICEM 2010*, IEEE, 2010, pp. 1–4.

[27] A. Y. B. Sasi, F. Gu, Y. Li, and A. D. Ball, "A validated model for the prediction of rotor bar failure in squirrel-cage motors using instantaneous angular speed," *Mechanical Systems and Signal Processing*, vol. 20, no. 7, pp. 1572–1589, 2006.

[28] L. O. A. Affonso, *Machinery failure analysis handbook: sustain your operations and maximize uptime*. Elsevier, 2013.

[29] R. P. Linessio, K. de Morais Sousa, T. Da Silva, C. A. Bavastri, P. F. da Costa Antunes, and J. C. C. Da Silva, "Induction motors vibration monitoring using a biaxial optical fiber accelerometer," *IEEE Sensors Journal*, vol. 16, no. 22, pp. 8075–8082, 2016.

[30] K. M. Sousa, U. J. Dreyer, C. Martelli, and J. C. C. da Silva, "Dynamic eccentricity induced in induction motor detected by optical fiber bragg grating strain sensors," *IEEE Sensors Journal*, vol. 16, no. 12, pp. 4786–4792, 2016.

[31] K. de Morais Sousa, A. A. Hafner, H. J. Kalinowski, and J. C. C. da Silva, "Determination of temperature dynamics and mechanical and stator losses relationships in a three-phase induction motor using fiber bragg grating sensors," *IEEE Sensors Journal*, vol. 12, no. 10, pp. 3054–3061, 2012.

[32] S. Misra, S. Kumar, S. Sayyad, A. Bongale, P. Jadhav, K. Kotecha, A. Abraham, and L. A. Gabralla, "Fault detection in induction motor using time domain and spectral imaging-based transfer learning approach on vibration data," *Sensors*, vol. 22, no. 21, p. 8210, 2022.

[33] G. Bossio, C. De Angelo, C. Pezzani, J. Bossio, and G. Garcia, "Evaluation of harmonic current sidebands for broken bar diagnosis in induction motors," in *2009 IEEE International Symposium on Diagnostics for Electric Machines, Power Electronics and Drives*, IEEE, 2009, pp. 1–6.

[34] G. Didier, E. Ternisien, O. Caspary, and H. Razik, "A new approach to detect broken rotor bars in induction machines by current spectrum analysis," *Mechanical Systems and Signal Processing*, vol. 21, no. 2, pp. 1127–1142, 2007.

[35] K. O. Hill and G. Meltz, "Fiber bragg grating technology fundamentals and overview," *Journal of lightwave technology*, vol. 15, no. 8, pp. 1263–1276, 1997.

[36] A. Othonos, "Fiber bragg gratings," *Review of scientific instruments*, vol. 68, no. 12, pp. 4309–4341, 1997.

[37] T. Li, J. Guo, Y. Tan, and Z. Zhou, "Recent advances and tendency in fiber bragg grating-based vibration sensor: A review," *IEEE Sensors Journal*, vol. 20, no. 20, pp. 12 074–12 087, 2020.

[38] G. Rajan, *Optical fiber sensors: advanced techniques and applications*. CRC press, 2017.

[39] Y. J. Rao, P. J. Henderson, D. A. Jackson, L. Zhang, and I. Bennion, "Simultaneous strain, temperature and vibration measurement using a multiplexed in-fibre-bragg-grating/fibre-fabry-perot sensor system," *Electronics letters*, vol. 33, no. 24, pp. 2063–2064, 1997.

[40] A. G. Leal-Junior, C. A. Dıaz, A. Frizera, C. Marques, M. R. Ribeiro, and M. J. Pontes, "Simultaneous measurement of pressure and temperature with a single fbg embedded in a polymer diaphragm," *Optics & Laser Technology*, vol. 112, pp. 77–84, 2019.

[41] Y. Qiu, Q.-b. Wang, H.-t. Zhao, J.-a. Chen, and Y.-y. Wang, "Review on composite structural health monitoring based on fiber bragg grating sensing principle," *Journal of Shanghai Jiaotong University (Science)*, vol. 18, pp. 129–139, 2013.

[42] H.-W. Ho, W.-H. Liao, C.-Y. Chang, and C.-C. Ma, "Structural health monitoring of a linear robot by fiber bragg grating sensors and cyber-physical system," *The International Journal of Advanced Manufacturing Technology*, vol. 122, no. 9-10, pp. 3983–3995, 2022.

[43] R. Kashyap, *Fiber bragg gratings*. Academic press, 2009.

[44] G. Strang, "Wavelets," *American Scientist*, vol. 82, no. 3, pp. 250–255, 1994.

[45] P. Welch, "The use of fast fourier transform for the estimation of power spectra: A method based on time averaging over short, modified periodograms," *IEEE Transactions on audio and electroacoustics*, vol. 15, no. 2, pp. 70–73, 1967.

[46] R. Cavalcanti, *Diagnoses algorithm*, https://github.com/rafaelmancuso/Master-s-Degree-in-Industrial-Engineering..git, 2023.

Appendix A

Algoritmo

The algorithm employed can be observed by accessing the GitHub directory [46]

```
# pip install -U apread
from sklearn import svm
import pandas as pd
import numpy as np
import statsmodels.api as sm
from mpl_toolkits import mplot3d
import matplotlib.pyplot as plt
import seaborn as sb
from sklearn.metrics import mean_squared_error, r2_score
from sklearn.model_selection import StratifiedShuffleSplit
from sklearn.metrics import mean_absolute_error
import glob

# To import new files from PC
# from google.colab import files
# uploaded = files.upload()

# To mount a Google Drive folder w/ data (lim max 90min or 12h)
from google.colab import drive
drive.mount('/content/drive/')

# Original data folder
# /content/drive/MyDrive/IPB/DD-UTFPR/2022-RafaelMancuso/TESE/Ensaios Barra
# quebrada/DataSet_orig/COPEL_100__BARRA_QUEBRADA
```

```
path_files = '/content/drive/MyDrive/TESE/Algoritmos/trabalhando/Ensaios_primitivos/'
# All files ending with .txt
files = glob.glob(path_files + '*.bin')
# print(files)
print("Names: {}".format(len(files)))

# CATMAN API https://github.com/leonbohmann/apreader (https://pypi.org/project/apread/)
db1 = 'COPEL_100__RotorBom.bin'
db2 = 'COPEL_100__BarraQuebrada.bin'
db3 = 'COPEL_75__BarraQuebrada.bin'
db4 = 'Gerador_100__RotorBom.bin'
db5 = 'Gerador_75__BarraQuebrada.bin'
db6 = 'Gerador_100__BarraQuebrada.bin'
db7 = 'COPEL_100__RotorBom.bin'

from apread import APReader
reader1 = APReader(path_files + db1)   # this will read in the file
reader2 = APReader(path_files + db2)
reader3 = APReader(path_files + db3)
reader4 = APReader(path_files + db4)
reader5 = APReader(path_files + db5)
reader6 = APReader(path_files + db6)
reader7 = APReader(path_files + db7)


# Reading all the files that contain the motor data, collected in different
# statuses, and putting in the format so it's possible to analyse.

#COPEL_100__RotorBom
print('\n' + db1)
print('\nGroups:')
for group1 in reader1.Groups:
  print(group1)

print('\nChannels:')
for i, channel in enumerate(reader1.Channels):
  print(i, channel)
channels1_8_16 = reader1.Channels[8:16]
for i, channel in enumerate(channels1_8_16):
    locals()["channelC100B_" + str(i+8)] = channel

#COPEL_100__BarraQuebrada
print('\n' + db2)
```

```
print('\nGroups:')
for group2 in reader2.Groups:
  print(group2)


print('\nChannels:')
for i, channel in enumerate(reader2.Channels):
  print(i, channel)
channels2_14_21 = reader2.Channels[14:22]
for i, channel in enumerate(channels2_14_21):
    locals()["channelC100Q_" + str(i+14)] = channel
    #print("channelC100Q_" + str(i+14), channel)


#COPEL_75__BarraQuebrada
print('\n' + db3)
print('\nGroups:')
for group3 in reader3.Groups:
  print(group3)

print('\nChannels:')
for i, channel in enumerate(reader3.Channels):
  print(i, channel)

channels3_14_21 = reader3.Channels[14:22]
for i, channel in enumerate(channels3_14_21):
    locals()["channelC75Q_" + str(i+14)] = channel
    #print("channelC75Q_" + str(i+14), channel)


#Gerador_100__RotorBom
print('\n' + db4)
print('\nGroups:')
for group4 in reader4.Groups:
  print(group4)

print('\nChannels:')
for i, channel in enumerate(reader4.Channels):
  print(i, channel)

channels4_8_15 = reader4.Channels[8:16]
for i, channel in enumerate(channels4_8_15):
    locals()["channelG100B_" + str(i+8)] = channel
```

```
    #print("channelG100B_" + str(i+8), channel)

#Gerador_75__BarraQuebrada
print('\n' + db5)
print('\nGroups:')
for group5 in reader5.Groups:
  print(group5)

print('\nChannels:')
for i, channel in enumerate(reader5.Channels):
  print(i, channel)

channels5_14_21 = reader5.Channels[14:22]
for i, channel in enumerate(channels5_14_21):
    locals()["channelG75Q_" + str(i+14)] = channel
    #print("channelG75Q_" + str(i+14), channel)


#Gerador_100__BarraQuebrada
print('\n' + db6)
print('\nGroups:')
for group6 in reader6.Groups:
  print(group6)

print('\nChannels:')
for i, channel in enumerate(reader6.Channels):
  print(i, channel)

channels6_14_21 = reader6.Channels[14:22]
for i, channel in enumerate(channels6_14_21):
    locals()["channelG100Q_" + str(i+14)] = channel
    #print("channelG100Q_" + str(i+14), channel)

#COPEL_100__RotorBom
print('\n' + db7)
print('\nGroups:')
for group7 in reader7.Groups:
  print(group7)

print('\nChannels:')
for i, channel in enumerate(reader7.Channels):
  print(i, channel)
```

```
channels7_8_15 = reader7.Channels[8:16]
for i, channel in enumerate(channels7_8_15):
    locals()["channelC100B_" + str(i+8)] = channel
    #print("channelC100B_" + str(i+8), channel)


def fft_unilateral(sinal):
    # Calculate the unilateral FFT of the signal
    Y = np.fft.fft(sinal)
    n = len(sinal)
    P2 = np.abs(Y / n)
    P1 = P2[:n//2+1]
    P1[1:-1] = 2*P1[1:-1]
    return P1

# This function localise the main component that shopuld be near 30Hz,
 # and the power associated with it.
def localizacao_componentes(componente_30):
    tempo_desejado1=componente_30-1;
    posicao_do_tempo1=8193*tempo_desejado1/500


    tempo_desejado2=componente_30+1;
    posicao_do_tempo2=8193*tempo_desejado2/500

    teste_recortadox=f[int(posicao_do_tempo1):int(posicao_do_tempo2)];
    teste_recortado=data_fft[int(posicao_do_tempo1):int(posicao_do_tempo2)];

    y=np.where(teste_recortado == max(teste_recortado));
    x=teste_recortadox[y].dot(1)[0];
    z=sum(teste_recortado) / len(teste_recortado)
    a=max(teste_recortado)<=z+10
    return max(teste_recortado),x,z,a

componente_120=120;

# This function localises the main component that should be near 120Hz
 # and the power associated with it.
def localizacao_componente_120(componente_120):
    #Trimming frequency intervals.
    tempo_desejado_120=componente_120-10;
    posicao_do_tempo_120=8193*tempo_desejado_120/500;
    tempo_desejado_120_2=componente_120+10;
```

```
    posicao_do_tempo_120_2=8193*tempo_desejado_120_2/500;

#Extracting power and frequency data along with the address of the desired #frequency data.
    teste_recortado_120=data_fft[int(posicao_do_tempo_120):int(posicao_do_tempo_120_2)];
    f_recortado_120=f[int(posicao_do_tempo_120):int(posicao_do_tempo_120_2)];

#Calculating the position of the main component around 120 Hz and the respective power.

    ceva= np.where(teste_recortado_120 == max(teste_recortado_120))
    valor_c120=f_recortado_120[ceva]
    ceva= sum(ceva)
    r = f_recortado_120[ceva].item()
    c = teste_recortado_120[ceva].item()
    global count_discarded_120

#making the count if the data is discarded or not.
    if not (118 <= r <= 122) or not (-60 <= c <= 0):

      count_discarded_120 += 1
      return None

# Locating the symmetrical components around 120 Hz, if they exist,
 # in order to analyze the power and the component

    localizacao_componente_120_negativa=np.where(teste_recortado_120[0:int(ceva-10)] == max(teste_recor
    teste_recortado_120[localizacao_componente_120_negativa]
    valor_c120n=f_recortado_120[localizacao_componente_120_negativa]
    localizacao_componente_120_positiva=np.where(teste_recortado_120[int(ceva+45):] == max(teste_recorta
    localizacao_componente_120_positiva=localizacao_componente_120_positiva+ceva+45
    valor_c120pm=f_recortado_120[localizacao_componente_120_positiva]
    media_valores_120=sum(teste_recortado_120) / len(teste_recortado_120)

    a=teste_recortado_120[localizacao_componente_120_positiva]<=media_valores_120+10
    b=teste_recortado_120[localizacao_componente_120_negativa]<=media_valores_120+10

    x=teste_recortado_120[localizacao_componente_120_positiva]
    y=f_recortado_120[localizacao_componente_120_positiva]

    w=teste_recortado_120[localizacao_componente_120_negativa]
    z=f_recortado_120[localizacao_componente_120_negativa]

    r=f_recortado_120[ceva]
    c=teste_recortado_120[ceva]
```

```
    valor_c120p=(2*valor_c120-(valor_c120n))

    return r,c,0,x,y,a,0,w,z,b,valor_c120p


# cleand data and close windows
plt.close('all')

fraction_split=2**14


# load data to make the final calculations.
t = 0.001
n=fraction_split

count1=0


r_values=[]
global count_discarded_30
count_discarded_120 = 0
count_discarded_30 = 0

# initialise the processes with a channel.
for i in channels4_8_15:

  m=i[50:]
  pp=len(m)/fraction_split
  x=m[:fraction_split*int(pp)]
  Dados_fracionados=np.split(x,int(pp))
  print("leitura"+str(i))

  for s1_corte in Dados_fracionados:
      # FFT calculations
      n = len(s1_corte)
      Fs = 1000
      f = Fs * np.arange(n//2+1) / n
      fft_result = fft_unilateral(s1_corte)
      data_fft=20*np.log10(fft_result)
      tempo_desejado1=20;
```

```
        posicao_do_tempo1=8193*tempo_desejado1/500;

        tempo_desejado2=40;
        posicao_do_tempo2=8193*tempo_desejado2/500;

# Locating the symmetrical components around 60 Hz, if they exist,
 #in order to analyze the power and the component

        teste_recortado=data_fft[int(posicao_do_tempo1):int(posicao_do_tempo2)];
        f_recortado=f[int(posicao_do_tempo1):int(posicao_do_tempo2)];
        max_value=max(teste_recortado);
        y=np.where(teste_recortado == max_value);
        velocidade_medida=f_recortado[y].dot(1)[0];
        potencia_velocidade_medida=teste_recortado[y]


        if not (27 <= velocidade_medida <= 33) or not (-60 <= potencia_velocidade_medida <= 0):

          count_discarded_30 += 1
          print("Leitura descartada 30",count_discarded_30)
          break

        velocidade_sincrona=30
        velocidade_acionamento=60
        escorregamento=(velocidade_sincrona-velocidade_medida)/velocidade_sincrona
        componente_positiva=velocidade_medida+(2*escorregamento*velocidade_acionamento)
        componente_negativa=velocidade_medida-(2*escorregamento*velocidade_acionamento)
        b=localizacao_componentes(componente_positiva)
        c=localizacao_componentes(componente_negativa)


        r_info = localizacao_componente_120(componente_120)


         #Plotting the graphs, if desired for checking.
        if r_info is not None:

          fig, axs = plt.subplots(2, 1)
          axs[0].plot(f, 20*np.log10(fft_result))
          axs[0].set_xlim([110, 130])
          axs[0].set_ylim([-125,-40])
          axs[1].plot(f, 20*np.log10(fft_result))
          axs[1].set_xlim([15, 45])
```

```
axs[1].set_ylim([-125,-40])
axs[0].set_xlabel('Frequência (Hz)', fontsize=10)
axs[0].set_ylabel('Potência (dB)', fontsize=10)
axs[1].set_xlabel('Frequência (Hz)', fontsize=10)
axs[1].set_ylabel('Potência (dB)', fontsize=10)
plt.subplots_adjust(hspace=0.5)
```